Depth-Varying Friction on a Ramp-Flat Fault Illuminated by ~3-Year InSAR Observations Following the 2017 Mw 7.3 Sarpol-e Zahab Earthquake

Zelong Guo[1,2] , Mahdi Motagh[1,2] , Jyr-Ching Hu[3] , Guangyu Xu[4], Mahmud Haghshenas Haghighi[2] , Abbas Bahroudi[5], Aram Fathian[6] , and Shaoyang Li[7]

[1]Department of Geodesy, GFZ German Research Centre for Geosciences, Section of Remote Sensing, Potsdam, Germany, [2]Institute for Photogrammetry and GeoInformation, Leibniz University Hannover, Hannover, Germany, [3]Department of Geosciences, National Taiwan University, Taipei, Taiwan, [4]Faculty of Geomatics, East China University of Technology, Nanchang, China, [5]Exploration Department, School of Mining Engineering, Engineering Faculty, University of Tehran, Tehran, Iran, [6]Neotectonics and Natural Hazards Institute, RWTH Aachen University, Aachen, Germany, [7]State Key Laboratory of Lithospheric Evolution, Institute of Geology and Geophysics, Chinese Academy of Sciences, Beijing, China

Abstract We use interferometric synthetic aperture radar observations to investigate the fault geometry and afterslip evolution within 3 years after a mainshock. The postseismic observations favor a ramp-flat structure in which the flat angle should be lower than 10°. The postseismic deformation is dominated by afterslip, while the viscoelastic response is negligible. A multisegment, stress-driven afterslip model (hereafter called the SA-2 model) with depth-varying frictional properties better explains the spatiotemporal evolution of the postseismic deformation than a two-segment, stress-driven afterslip model (hereafter called the SA-1 model). Although the SA-2 model does not improve the misfit significantly, this multisegment fault with depth-varying friction is more physically plausible given the depth-varying mechanical stratigraphy in the region. Compared to the kinematic afterslip model, the mechanical afterslip models with friction variation tend to underestimate early postseismic deformation to the west, which may indicate more complex fault friction than we expected. Both the kinematic and stress-driven models can resolve downdip afterslip, although it could be affected by data noise and model resolution. The transition depth of the sedimentary cover basement interface inferred by afterslip models is ~12 km in the seismogenic zone, which coincides with the regional stratigraphic profile. Because the coseismic rupture propagated along a basement-involved fault while the postseismic slip may activate the frontal structures and/or shallower detachments in the sedimentary cover, the 2017 Sarpol-e Zahab earthquake may have acted as a typical event that contributed to both thick- and thin-skinned shortening of the Zagros in both seismic and aseismic ways.

Plain Language Summary The 2017 Mw 7.3 Sarpol-e Zahab earthquake is the largest instrumentally recorded event to have ruptured in the Zagros fold thrust belt. Although much work has been conducted for a better understanding of the relationship between crustal shortening and seismic and aseismic slip of the earthquakes in the Zagros, active debate remains. Here, we use interferometric synthetic aperture radar observations to study the fault geometry and afterslip evolution within 3 years after the 2017 Mw 7.3 Sarpol-e Zahab earthquake. For postseismic deformation sources, afterslip and viscoelastic relaxation are considered to be possible causes of postseismic deformation. Our results show that the kinematic afterslip model can spatiotemporally explain the postseismic deformation. However, the mechanical afterslip models tend to underestimate the earlier western part of the postseismic deformation, which may indicate a more complex spatial heterogeneity of the frictional property of the fault plane. We find that there is deep afterslip downdip of coseismic slip from both the kinematic and stress-driven afterslip models, although it could be affected by data noise and model resolution. We additionally find that the viscoelastic response is negligible. Postseismic slip on more complex geological structures may also be reactivated and triggered, combined with geodetic inversions, geological cross-section data and local structures in the Zagros.

1. Introduction

The ongoing collision between the Eurasian and Arabian plates has led to the formation of one of the most tectonically and seismically active intracontinental orogens: the northwest-southeast striking Zagros Mountains in southwestern Iran. The convergence velocity between the Eurasian and Arabian plates is ~2–3 cm yr⁻¹, almost
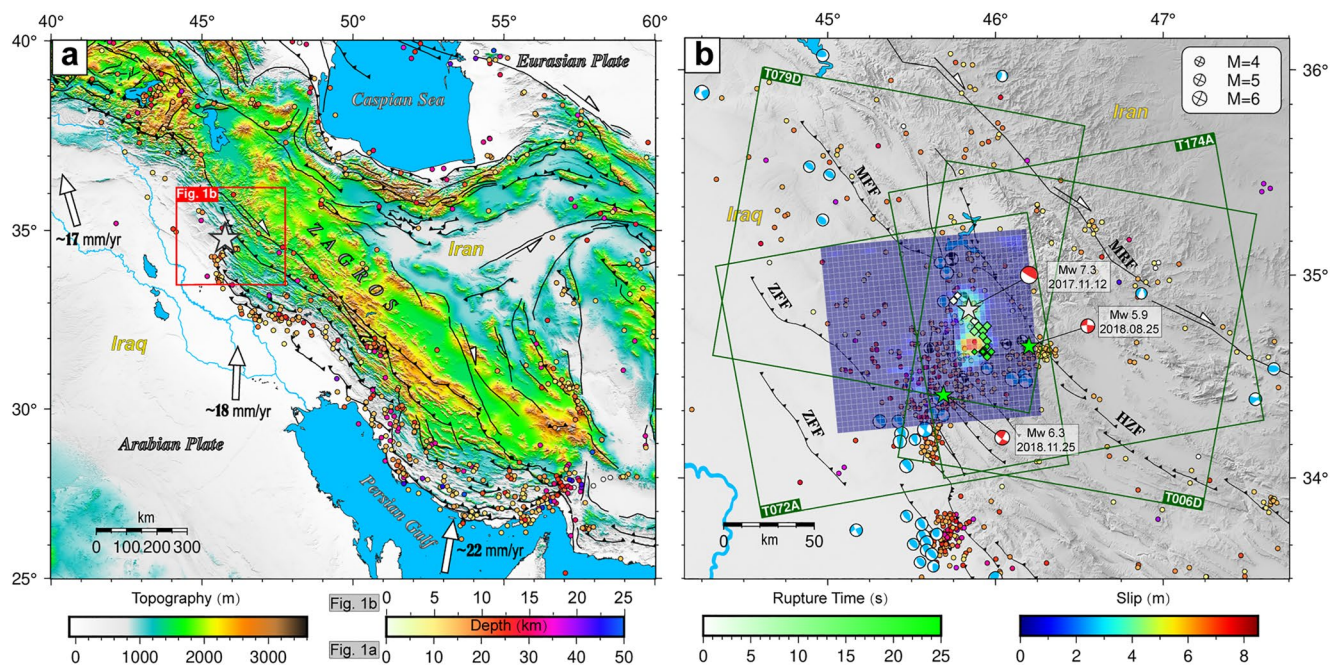
Figure 1. (a) Tectonic background of the 2017 Sarpol-e Zahab earthquake. The colored dots are earthquakes (from 1976 to 2021) from the Global Centroid Moment Tensor (GCMT) catalog (https://www.globalcmt.org). (b) Detailed tectonic map of the seismogenic area. The blue beach balls are from the GCMT catalog. Colored dots are earthquakes (from 2006 to 2021 with $M > 3.5$) from the Iranian Seismological Center (IRSC, http://irsc.ut.ac.ir). Dark green boxes indicate the spatial extent of Sentinel-1 imagery used in this study. The coseismic slip distribution is from the ramp-flat fault model (see Section 4.1). Black beach balls are from Nissen et al. (2019). Red beach balls are the focal mechanisms of the 2017 Sarpol-e Zahab mainshock and two ~M 6 aftershocks. The green rhombuses represent the rupture time of the mainshock, which is mapped from Nissen et al. (2019). ZFF: Zagros Foredeep Fault; MRF: Main Recent Fault; HZF: High Zagros Fault; and MFF: Mountain Front Fault.

half of which is accommodated by the Zagros mountain belt (Figure 1a; e.g., Khorrami et al., 2019; Vernant et al., 2004). In northwestern Zagros, the deformation rate is partitioned as ~5 mm yr^{-1} dextral strike-slip motion along northwest-southeast trending faults, and ~4 mm yr^{-1} shortening perpendicular to the mountain belt, while in southeastern Zagros, the deformation is ~9 mm yr^{-1} pure shortening perpendicular to the belt (Walpersdorf et al., 2006). Contemporary active deformation around the Zagros Fold Thrust Belt (ZFTB) is mainly derived from seismic and aseismic deformation triggered by thrust and strike-slip faulting (e.g., Barnhart & Lohman, 2013; Copley et al., 2015; Motagh et al., 2015), folding and uplift of sedimentary cover (e.g., Berberian, 1995), and ductile thickening of the basement (Allen et al., 2013). The Phanerozoic sedimentary cover rock reaches a thickness of ~8–13 km, overlying the Phanerozoic crystalline basement. Much work has been done to explore thin- and thick-skinned shortening related to the Phanerozoic sedimentary succession and deep basement faulting in the Zagros belt (e.g., Falcon, 1969; Molinaro et al., 2005; Mouthereau et al., 2012; Talebian & Jackson, 2004). Moderate magnitude earthquakes (~M 5–6) have been widely distributed in the ZFTB, but the characterization and contribution of such seismicity to cover basement interaction are still not fully understood (e.g., Copley et al., 2015; Motagh et al., 2015; Nissen et al., 2011; Talebian & Jackson, 2004). A Hormuz salt unit in Fars Arc and shales in the Lurestan Arc due to the strong mechanical contrast between sedimentary cover and basement are suspected as a decoupling layer at the cover basement interface (e.g., Alavi, 2007; McQuarrie, 2004), which may impede propagation of fault ruptures to the surface in this region. Under such a geological and tectonic environment, many blind thrust faults that cut through the sedimentary cover, grow in the ZFTB and contribute to the current topography of the Zagros. The major faults within the ZFTB consist of the Main Recent Fault, the Mountain Front Fault (MFF), the High Zagros Fault (HZF), and the Zagros Foredeep Fault (ZFF) (Berberian, 1995, Figure 1b).

On 12 November 2017 at 18:18 UTC, an earthquake with a magnitude of Mw 7.3 and focal depth of approximately 21 km struck ~50 km north of Sarpol-e Zahab city, in Kermanshah Province in western Iran, which is also very close to the Iran and Iraq border (Figure 1). The main event occurred along a shallowly east-dipping reverse fault with dextral components in the Lurestan Arc of the ZFTB and is the largest earthquake in this

region since instrumental records began recording. Several ~M 6 earthquakes in the sedimentary cover followed the mainshock, such as the 25 August 2018 Mw 5.9 event, and 25 November 2018 Mw 6.3 event (Figure 1b). However, these two large aftershocks along steeply dipping dextral strike-slip faults may reveal strain partitioning in the northwestern Zagros belt as the overall convergence direction between the Eurasian and Arabian plates changes from orthogonal shortening in southeastern Zagros to oblique shortening in northwestern Zagros (e.g., Talebian & Jackson, 2004). The 2017 Sarpol-e Zahab mainshock is located in a crystalline basement, where the seismicity interactions between sedimentary cover and basal basement due to the possible existence of the weak Hormuz shale as a decoupled layer is still an open question (e.g., Barnhart et al., 2018; Nissen et al., 2011; Wang & Bürgmann, 2020).

Several studies have been performed to better understand the seismic and aseismic slip of the 2017 Sarpol-e Zahab earthquake using geodetic observations, but some debate still remains, for example, the number of coseismic slip asperities (e.g., Feng et al., 2018; Nissen et al., 2019; Vajedian et al., 2018; Yang et al., 2018), the existence of downdip afterslip (e.g., Liu & Xu, 2019; Wang & Bürgmann, 2020) and the postseismic contribution from viscoelastic relaxation (e.g., Barnhart et al., 2018; Lv et al., 2020; Wang & Bürgmann, 2020). In this study, we extend earlier studies and investigate both co- and postseismic models of the 2017 Mw 7.3 Sarpol-e Zahab event with interferometric synthetic aperture radar (InSAR) data. First, we analyze the optimal coseismic fault model from planar and a range of listric faults with coseismic interferograms; checkerboard resolution tests are also performed to test the sensitivity of observations to multiple slip asperities. Then, we process ~3 years of Sentinel-1 data to derive the postseismic deformation time series and study the fault geometry and transient aseismic slip evolution for the first 4, 7, 10, 12, 24, and 36 months after the mainshock. We also analyze the deep afterslip downdip of the coseismic rupture from the perspective of data accuracy and model resolution, as well as the postseismic contribution from the viscoelastic response. Finally, we discuss the complexity of fault friction, the reactivation of the MFF system and/or shallower multiple detachments that were most likely triggered by the mainshock, given our inversion results and the structural geology background of the Zagros.

2. InSAR Observations

2.1. Data Analysis

Four tracks of Sentinel-1 single look complex (SLC) data cover the seismogenic zone of the 2017 event (Figure 1b). The SLC data from two ascending tracks (T072A and T174A) and two descending tracks (T006D and T079D) are processed with GAMMA software (Wegmüller et al., 2015). The topography effect is removed by a 30-m (1 arc sec) Digital elevation model (DEM) from the Shuttle Radar Topography Mission (SRTM; Farr et al., 2007). A 10 by 2 multilook factor for range and azimuth directions are performed to improve the signal to noise ratio. Generic Atmospheric Correction Online Service (GACOS) for InSAR products (Yu et al., 2018) are used to reduce atmospheric delay error from differential interferograms (Table S1 and Figure S1 in Supporting Information S1). The full variance-covariance matrix (VCM), constructed using a 1-D exponential covariance function with far-field nondeforming area in coseismic interferograms (Feng et al., 2013), indicates that the far-field noise is less than 1 cm after atmospheric delay correction with GACOS.

To analyze postseismic deformation, we perform multitemporal interferometry analysis in four tracks of Sentinel-1 data based on the Small Baseline Subset (SBAS) technique (Berardino et al., 2002). We construct a network of high-coherence small baseline interferograms covering 3 years after the 2017 Sarpol-e Zahab earthquake (Table S2 in Supporting Information S1). The thresholds of 200 m and 50 days are selected for the spatial and temporal baselines (Figure S2 in Supporting Information S1). The SBAS method of StaMPS software (Hooper et al., 2007) is used for time series analysis after differential interferometric processing with GAMMA. The measurement points are selected using a coherence threshold of 0.3. After correcting for the atmospheric delay using GACOS products and the DEM errors, we finally obtain the InSAR time series and cumulative line-of-sight (LOS) displacements for 3 years following the 2017 event.

2.2. Co- and Postseismic Displacements

Coseismic interferograms from ascending data T072A and T174A suggest that the maximum and minimum LOS displacements are approximately 85 and −21 cm, respectively (surface motion toward the satellite is positive, Figure S1 in Supporting Information S1). For the descending data T006D and T079D, the maximum and

minimum LOS displacements are approximately 50 and −39 cm, respectively (Figure S1 in Supporting Information S1). The difference in the sense of range measurements between the ascending and descending tracks indicates a significant contribution from east-west coseismic deformation. The coseismic interferograms also contain information from early postseismic deformation because of the 12-day revisit time of the Sentinel-1 satellite.

As shown in Figures 2e–2f, the 3-year cumulative range changes at P1 and P2 are approximately 15 cm and −12 cm for ascending Track T072A and descending Track T006D, respectively. Note that in Figures 2a–2d, there is some localized signal contamination due to the co- and postseismic deformation of the two large aftershocks: the Mw 5.9 earthquake on 25 August 2018 and the Mw 6.3 earthquake on 25 November 2018 (Figures 1b and 2a–2d). In this study, the fault models of these two aftershocks proposed by Fathian et al. (2021) (Figures 2a–2d and Figure S3 in Supporting Information S1) are used for forward modeling, and then we take the difference between our original InSAR time series and the simulations to obtain a cleaner postseismic time series (Figures S3 and S4 in Supporting Information S1). In the following sections, the coseismic deformation of the two aftershocks is reduced from all of the time series influenced by these two large events (Figure S4 in Supporting Information S1) and is then employed for further analysis and inversions.

3. Coseismic Fault Models

The four coseismic interferograms (Figure S1 in Supporting Information S1) are downsampled with a quadtree sampling approach (Jónsson et al., 2002, Figure S5 in Supporting Information S1) to reduce the computation, and then the nonlinear global search is performed for the fault parameters (Text S1 and Figure S6 in Supporting Information S1). Afterward, we carry out linear inversions for the distributed slip on the fault plane (e.g., Xu et al., 2019). The fault geometry derived from nonlinear inversion is fixed, and we extend the along-strike fault length and along-downdip fault width to 100 km, before the fault plane is discretized to fault patches with 3 km by 3 km. We find that the fault model with a dip angle of 15° fits the coseismic displacements best from a variety of planar faults (Figure S7 in Supporting Information S1). We impose rake constraints from 110° to 160° and select 0.8 as the best-fitting smoothing factor for the planar fault (Figure S7 in Supporting Information S1).

Fathian et al. (2021) proposed a listric fault to model coseismic deformation based on relocated aftershocks, while other studies used a simple planar fault only (e.g., Barnhart et al., 2018; Feng et al., 2018; Wang & Bürgmann, 2020). Here, different from Fathian et al. (2021), we attempt to search for a listric fault model from the perspective of coseismic data fitting. We fix the upper fault depth at 13.4 km, which is derived from our nonlinear inversion, and then test a range of dip angles from 13° to 25° (hereafter called the initial dip) at this depth. We construct the following equation to constrain the fault:

$$
\mathrm{dip}_n =
\begin{cases}
a \cdot (13.4 - n) + \mathrm{dip}_{n+1}, & n < 13.4 \\
b, & n = 13.4 \\
-a \cdot (n - 13.4) + \mathrm{dip}_{n-1}, & n > 13.4
\end{cases}
, \; b \in [13, 25]
\tag{1}
$$

where n is the depth (km) of the fault patch; dip_n represents the dip angle of the fault patch at a depth of n km; a controls the curvature of the fault model ($a \in [0 : 0.2 : 8]$), b is the initial dip of the nonlinear-inversion upper fault boundary, where the depth is 13.4 km. Here, we test a range of initial dips for b from 13 to 25° with 1° intervals. A particular case is that the fault could be planar and the dip angle could be b if $a = 0$. The same smoothing factor and rake constraints with the abovementioned planar fault are imposed in the inversions. Our results show that, however, the best-fitting fault model is still a single planar fault dipping 15°, which can sufficiently explain the InSAR observations (Figure 3a). The misfit of the listric fault with $a = 4$, $b = 22°$ is not significantly worse than that of the planar fault dipping 15° (Figures 3a and 3c) because the fault geometries producing coseismic ruptures are very similar. Even though the coseismic slip favors a planar fault model, the postseismic slip along the listric fault may also be triggered when the MFF system is reactivated (see Section 5.4).

The coseismic slip model reveals a unilaterally southward rupture for the mainshock involving the sequential rupture of two asperities, along a dextral-thrust fault (Figure 3b). The main coseismic slip area is concentrated at a depth range of ∼13–19 km with maximum slip exceeding 7 m. The geodetic moment is estimated to be 1.0×10^{20} N m, corresponding to a moment magnitude of Mw 7.3. The surface deformation predicted by the coseismic
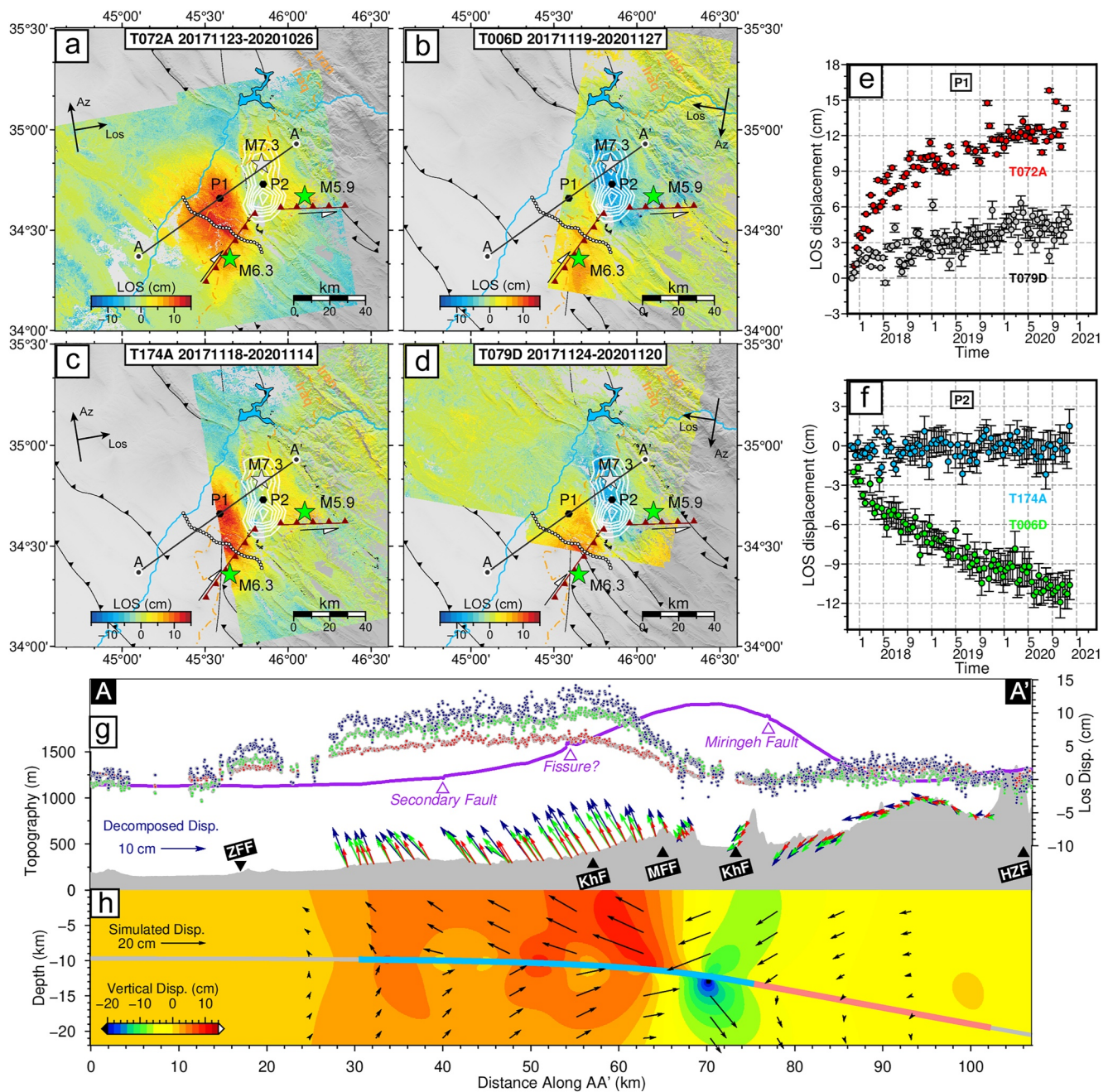
Figure 2. (a–d) The ~3-year cumulative postseismic line-of-sight (LOS) displacements of T072A, T006D, T174A, and T079D, respectively. White contours and gray stars represent our preferred coseismic slip model at 1-m intervals and the epicenter of the Mw 7.3 mainshock, respectively. Green stars and dark red faults represent the locations of the two large aftershocks and the corresponding fault traces from Fathian et al. (2021). White dots (black outline) are the surface trace of the secondary fault indicated by the coseismic interferogram discontinuity and field survey (Vajedian et al., 2018). Profile AA', which is nearly orthogonal to the geological structures, corresponds to the surface observations and simulations of Figure 7. (e–f) LOS displacement time series of P1 and P2, and the error bars are the standard deviations from pixels within a radius of 30 m. (g) Contribution of postseismic deformation to topography along Profile AA'. The red, green and dark blue dots represent the postseismic LOS displacements at 4 months, 1 year, and 3 years after the mainshock, respectively. The purple line indicates the coseismic LOS displacements, which are scaled by a factor of 5. The red, green and dark blue vectors are the 2.5-dimension deformation (quasi-eastward and quasi-upward) of 4 months, 1 year, and 3 years after the mainshock, respectively, which are decomposed from ascending Track T072A and descending Track T079D. (h) The 3-dimension displacements in depths along Profile AA', which is simulated from the 3-year kinematic afterslip model. The gray line indicates the ramp-flat fault proposed in Section 4.1, and the light red and light blue lines show the approximate scopes of coseismic rupture and postseismic afterslip, respectively. ZFF: Zagros Foredeep Fault; HZF: High Zagros Fault; and MFF: Mountain Front Fault.
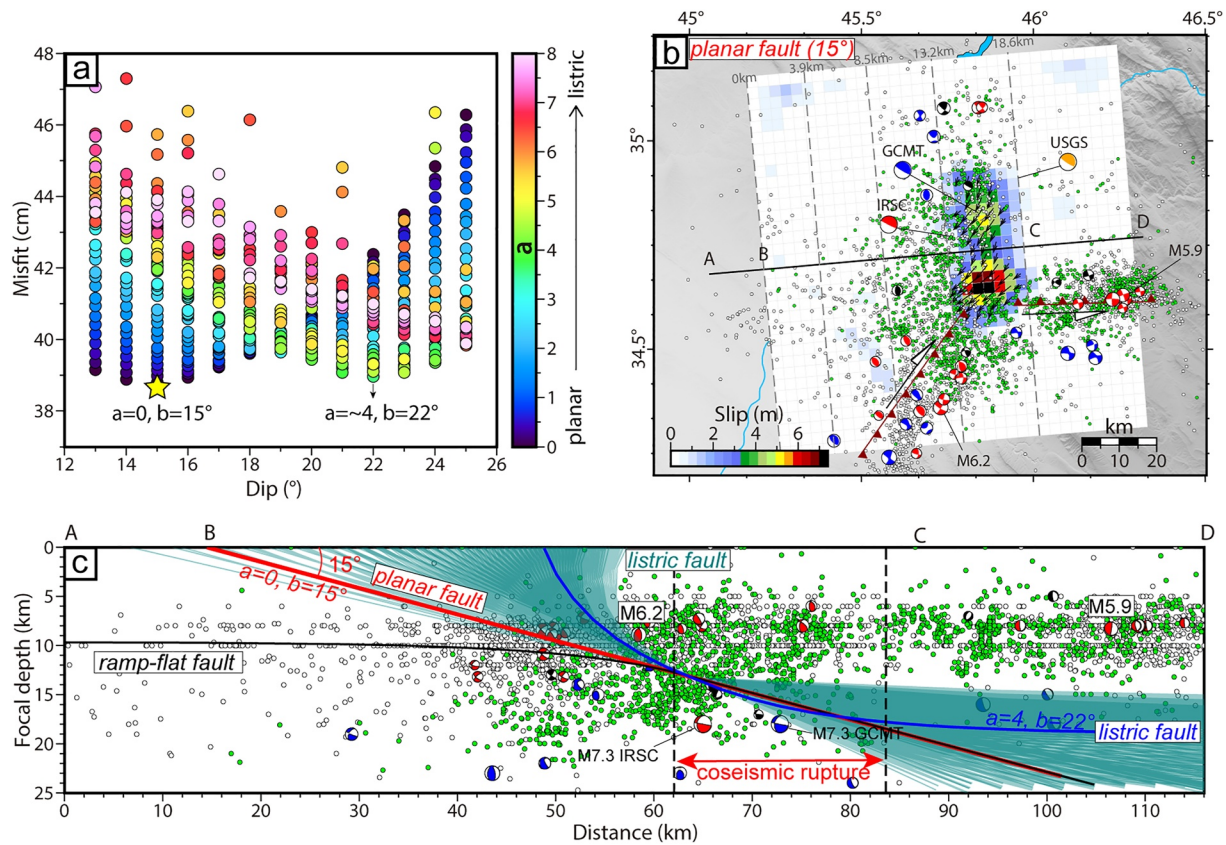
Figure 3. (a). The searched fault models with Equation 1. The optimal fault (yellow star) is a planar fault with a dip of 15°. (b) Slip distribution with the planar fault dipping 15°. The two dark red, strike-slip faults of the M 5.9 and M 6.3 events are from Fathian et al. (2021). (c) Seismicity projection of Profile AD in (b) along depth. The green and white dots indicate the relocated aftershocks within approximately 2 months from Fathian et al. (2021) and aftershocks within approximately 3 years from the Iranian Seismological Center (IRSC) catalog, respectively. The red, blue and black beach balls are the focal mechanisms from IRSC, Global Centroid Moment Tensor and Nissen et al. (2019), respectively. The cyan lines indicate all of the tested listric fault models. The red, blue and black lines are the planar fault model dipping 15°, the listric fault model with $a = 4$, $b = 22°$ and the ramp-flat model proposed in Section 4.1, respectively.

model is in good agreement with the observations (Figure S8 in Supporting Information S1). Our coseismic model confirms two asperities (Figure 3b), which is similar to the InSAR-derived results of some previous studies (e.g., Barnhart et al., 2018; Feng et al., 2018), while others proposed only one simple asperity (e.g., Wang & Bürgmann, 2020, Table S3 in Supporting Information S1). It is worth noting that a finite fault model from seismic waveforms and backprojection results also favor two apparent parts which produce separate peak slips and energy release (Nissen et al., 2019, Figure 1b). Checkerboard resolution tests are also performed to evaluate how sensitive the InSAR observations are to the slip asperities (see Text S2 and Figure S9 in Supporting Information S1). The checkerboard tests reveal that the InSAR observations in this study have a good recovery of coseismic slip distribution (Figure S9 in Supporting Information S1), and thus, we attribute the difference in asperity numbers in previous studies to the difference in fault parameterization (e.g., fault location and depth, see Table S3 in Supporting Information S1), inversion configurations (e.g., smooth factor) and input data among previous studies.

4. Postseismic Fault Models

In this section, we explore the fault structure based on kinematic afterslip inversions and search for an optimal mechanical afterslip model that features varied frictional properties along the fault plane. Then, we explore the possibility of the combination of stress-driven afterslip and viscoelastic relaxation as a possible postseismic model. Finally, a detailed analysis of the downdip afterslip is conducted. Here, we do not take the poroelastic rebound into consideration because the predicted poroelastic contribution 1 year after the 2017 mainshock was lower than 5 mm, and the spatial pattern of the simulations was in contrast to the postseismic observations (Wang & Bürgmann, 2020).
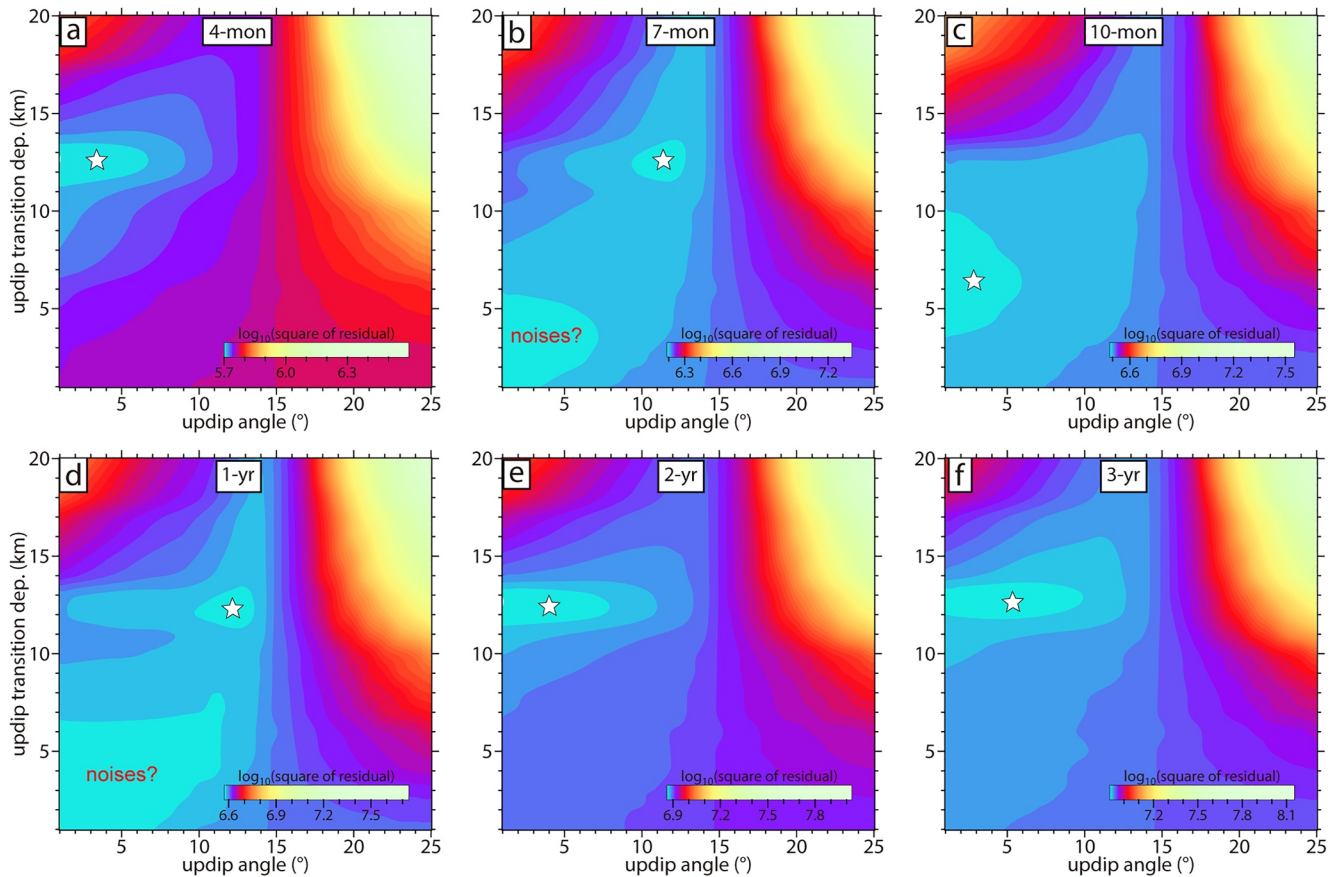
Figure 4. Misfit for searching the updip angles and transition depths with the postseismic observations 4, 7 and 10 months and 1, 2 and 3 years after the mainshock.

4.1. Fault Model Based on Kinematic Afterslip

Previous studies have suggested that the postseismic deformation of the 2017 Sarpol-e Zahab event was mainly dominated by afterslip, while the viscoelastic and poroelastic contributions were negligible (Barnhart et al., 2018; Wang & Bürgmann, 2020). Under such assumptions, they indicated that the mainshock and afterslip activated a ramp-and-flat structure. Here, we perform more detailed searches than previous studies to derive the fault structures with postseismic deformation of 4, 7, 10, 12, 24, and 36 months after the mainshock (Figure S4 in Supporting Information S1). We downsample the InSAR postseismic observations uniformly around the main deformation area (Figure S10 in Supporting Information S1) and seek a time-invariant fault geometry that is able to satisfactorily match the InSAR observations, given estimates of their uncertainties. Initially, we attempt to search for a flat-ramp-flat structure. We fixed the middle ramp part with a dip angle of 15°, and the angles of the updip and downdip flat part are allowed to vary above (4–16 km) and below (18–26 km) a certain depth, respectively (hereafter called the updip and downdip transition depths). Our results indicate that a wide range of downdip angles can fit the data equally well (Figure S11 in Supporting Information S1), which indicates that the data cannot resolve the downdip fault geometry well. However, both the kinematic and stress-driven afterslip models can identify the downdip afterslip, although it is much smaller than the updip afterslip (see Section 4.4 for more analysis about the downdip afterslip).

For the updip geometry, the results show that the updip angle should be lower than 15°, but the data have little resolution for the transition depth and dip angles smaller than 15° (Figure S11 in Supporting Information S1). To reduce the number of searching parameters, we fix the downdip angle to 15° so that there are only two variables (updip angle and transition depth), and we reselect the updip angle and transition depth. The results show that the updip angle and transition depth should be lower than 10° and ~12 km, respectively, based on the 4-month, 2-, and 3-year postseismic observations (Figures 4a, 4e and 4f). However, the updip geometry cannot be constrained very well by the postseismic observations at 7, 10 months, and 1 year after the event (Figures 4b–4d), which
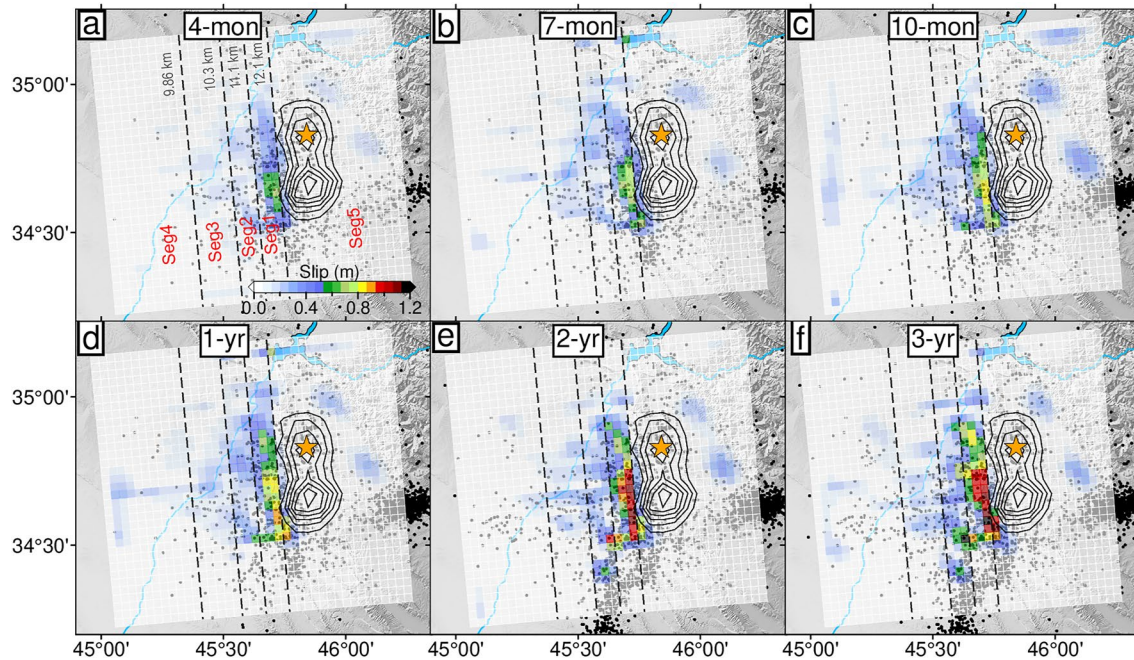
Figure 5. Spatiotemporal evolution of aftershocks and kinematic afterslip model. Black contours and orange stars represent the coseismic slip model at 1-m intervals and the epicenter of the Mw 7.3 mainshock, respectively. The black dots indicate that the aftershocks are from the Iranian Seismological Center catalog. The black dashed lines that divide the fault plane into five parts (seg1-5) represent the fault depth.

may be attributed to observation noise (Figure S12 in Supporting Information S1). Additional searches are also performed based on the 8-, 9-, 13-, and 15-month postseismic observations, the results are found to be similar with those of 4-month, 2-, and 3-year postseismic observations (Figure S13 in Supporting Information S1). In addition to the residual noises, considering the variations in transition depth, geological background and local stratigraphic profile, a more complex fault structure is likely to be triggered (see Section 5.4). Overall, most postseismic observations favor a ramp-flat structure in which the flat angle should be lower than 10°, but the refined structure of updip geometry cannot be resolved very well with InSAR observations.

Because it is difficult to make a compromise between the updip angle and upper transition depth, and considering the interface between the sedimentary cover and basement, we propose a ramp-flat fault (anti-listric fault, to be strict) model with a variable dip at depth with the following equation:

$$\text{dip}_n = \begin{cases} -4 \cdot (13.4 - n) + \text{dip}_{n+1}, & n < 13.4 \\ 15, & n \geq 13.4 \end{cases}$$ (2)

the symbols used, and their meanings, are the same as those in Equation 1. We adopted $a = -4$ (dip angle would be 0 at ~10 km) since the basement depth is approximately 8–13 km. Moreover, this ramp-flat fault is consistent with the aftershock locations updip of the coseismic rupture (Figure 3c), and this model strongly resembles the ramp-flat structure proposed by Barnhart et al. (2018) and Wang and Bürgmann (2020). The ramp-and-flat model can not only explain the postseismic deformation but can also produce a slightly smaller misfit (38.3 cm) for coseismic inversion than the planar model (38.9 cm). Therefore, we take the ramp-flat coseismic model (Figure S14 in Supporting Information S1) as our preferred model in the following inversions.

As shown in Figure 5, the afterslip model based on the ramp-flat fault is mainly concentrated updip of the coseismic rupture, despite some localized deep afterslip. The spatiotemporal evolution of the kinematic afterslip model agrees well with the aftershock locations updip of the fault, which indicates that the aftershocks may have been triggered by aseismic afterslip. The 3-year maximum kinematic afterslip is approximately 1.2 m, which is similar to that of the stress-driven afterslip model (Figure 6, see Section 4.2 for details). The cumulative moment release calculated from the 3-year afterslip model is approximately 2.6×10^{19} Nm, which is equivalent to the moment of
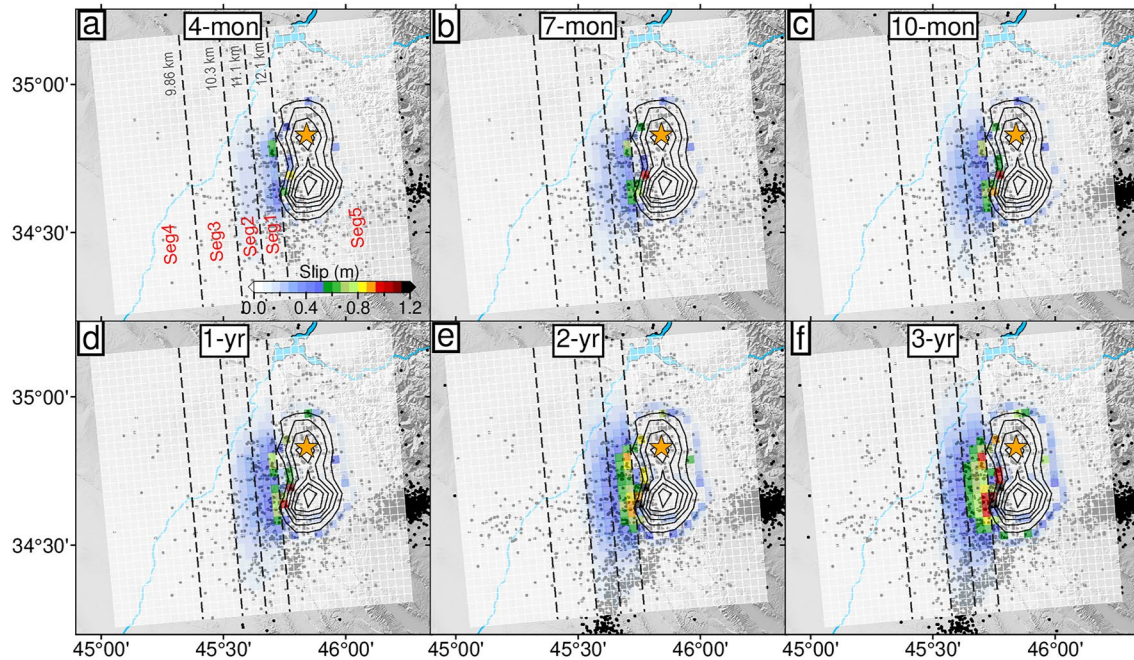
Figure 6. Spatiotemporal evolution of aftershocks and stress-driven afterslip Model 2 (SA-2 model). Black contours and orange stars represent the coseismic slip model at 1-m intervals and the epicenter of the Mw 7.3 mainshock, respectively. The black dots indicate that the aftershocks are from the Iranian Seismological Center catalog. The black dashed lines that divide the fault plane into five parts (seg1-5) represent the fault depth.

a Mw 6.9 earthquake. The kinematic afterslip model can predict the InSAR observations spatiotemporally well (Figure 7).

4.2. Stress-Driven Afterslip Simulation

We calculate the time-dependent evolution of rate-strengthening friction faults to coseismic stress change with the application of Unicycle codes (Barbot et al., 2017). The fault slip rate controlled by a purely rate-strengthening friction law can be shown as (e.g., Barbot et al., 2009):

$$V = 2V_0 \sin h \frac{\Delta \tau}{(a-b)\sigma} \tag{3}$$

This is a steady state simplification of the rate-and-state friction law (e.g., Marone, 1998; Marone et al., 1991), where V_0 and $a-b$ represent the reference slip rate before the coseismic shear stress changes $\Delta \tau$ are applied and frictional parameter of the material, respectively, and σ is the effective normal stress on the fault. Here V_0 does not correspond directly to the interseismic slip rate (Barbot et al., 2009). The steady state assumption is valid as the magnitude of the afterslip for the 2017 Sarpol-e Zahab earthquake ($>10^{-1}$ m) is greater than the laboratory-derived values of D_c which are on the order of 10^{-5} m (e.g., Marone, 1998). In our simulations, we select the main coseismic area at depths of ~12–20 km with coseismic slip >0.8 m as the Unicycle input model. V_0 and $(a-b)\sigma$, which are considered constitutive parameters, are searched based on the misfit between InSAR observations and simulations.

We search five parameters including V_0 and $(a-b)\sigma$ updip and downdip of the coseismic rupture and the transition depth where the fictional properties of fault rocks change. Initially, the 3-year postseismic deformation time series from the four tracks of Sentinel-1 images are used for searching the five parameters. We employ the simulated annealing algorithm (e.g., Kirkpatrick et al., 1983) to search the global optimal solutions of the constitutive parameters, but there is still a possibility of obtaining the local minima due to the complexity of the chosen parameters for simulated annealing. Thus, we perform a number of iterative operations with different chosen parameters of the algorithm, initial values and boundary constraints. The solution that yields the minimum data misfit is selected as the final optimal solution. The results show that the updip V_0 and $(a-b)\sigma$ are 0.078 m yr^{-1}
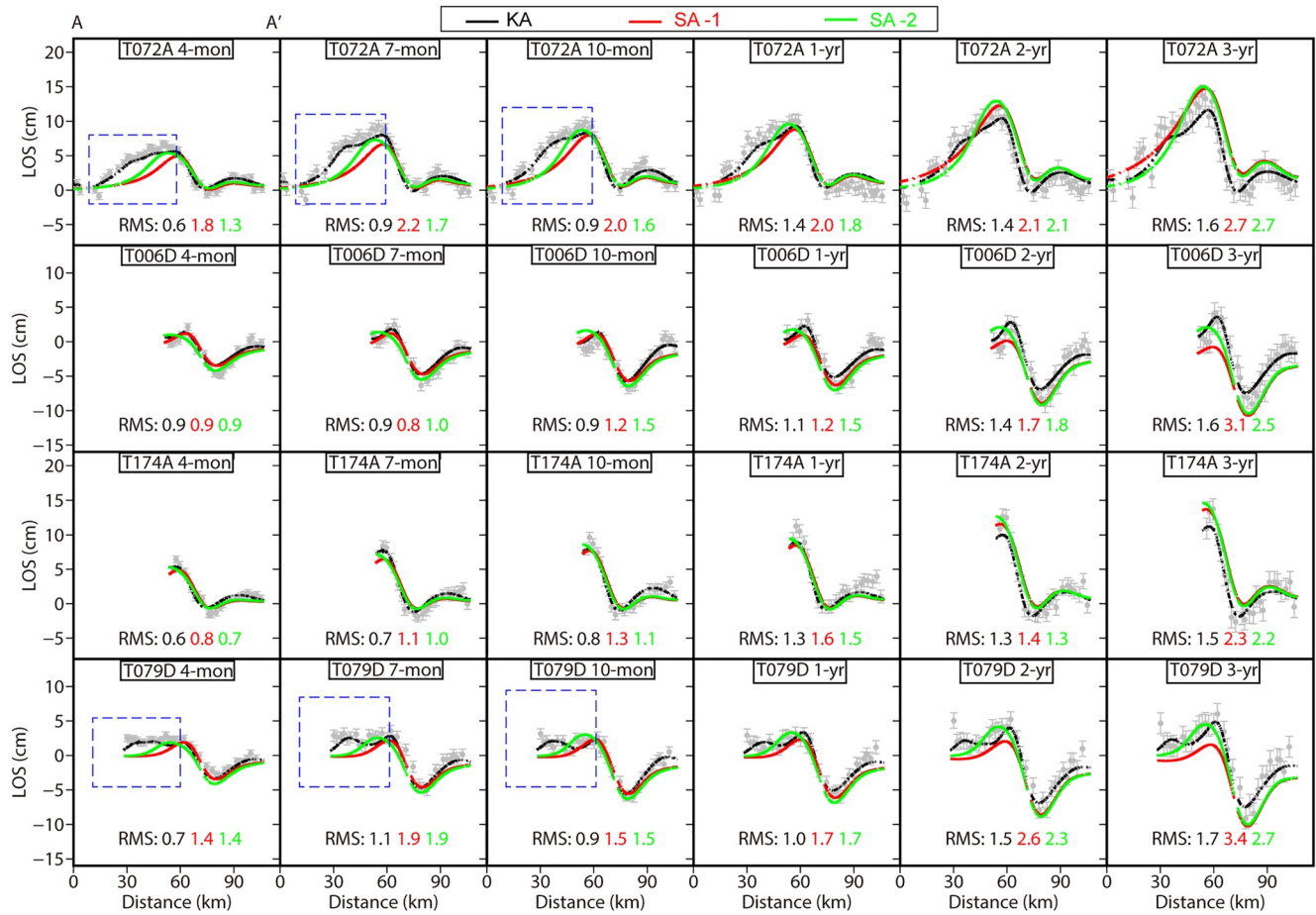
Figure 7. The fitting between interferometric synthetic aperture radar (InSAR) observations and simulations from 4 months to 3 years after the mainshock along Profile AA' in Figures 2a–2d. The gray error bars are based on the InSAR observations, which represent the far-field noise from variance-covariance matrix. The black, red and green lines represent the simulations from Kinematic Afterslip (KA) and Stress-driven Afterslip Model 1 (SA-1 model) and Stress-driven Afterslip model 2 (SA-2 model), respectively. The blue dashed boxes indicate the underfitting between observations and simulations from stress-driven afterslip models.

and 0.56 MPa, respectively; for the downdip part of the fault, V_0 and $(a - b)\sigma$ converge to 0.009 m yr⁻¹ and 1.84 MPa, respectively; the optimal transition depth is approximately 12.14 km (Table 1; Figure 8). This model (herein referred to as the SA-1 afterslip model, Figure S15 in Supporting Information S1) reflects the friction contrast between the updip and downdip sections of the fault and requires afterslip downdip of the coseismic

Table 1
Constitutive Parameters Derived From This Study and Previous Work

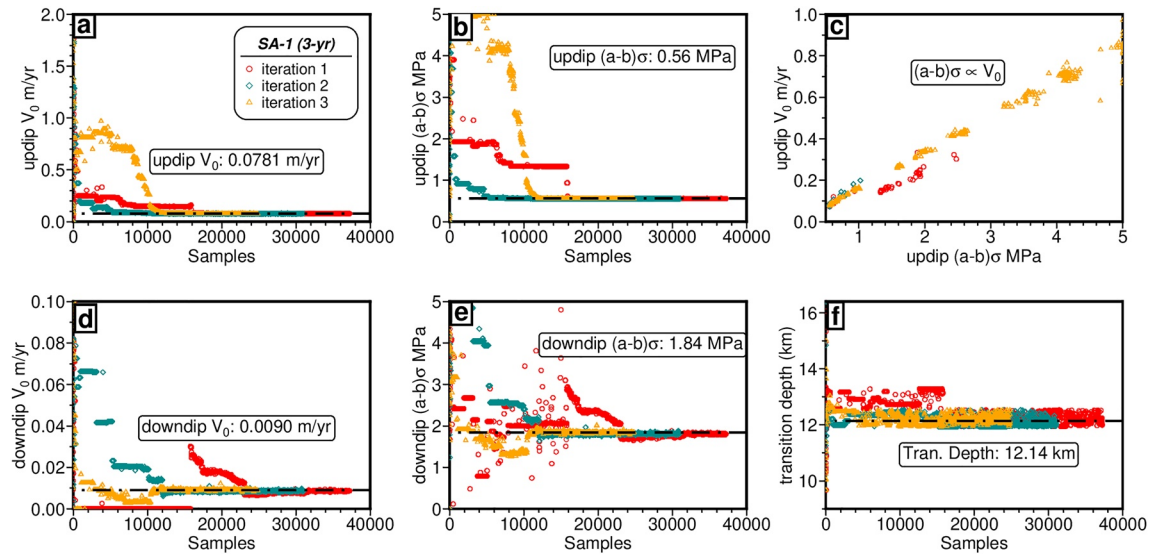| Postseismic data/Source	Updip flat		Downdip ramp		Transition depth (km)
	$(a - b)\sigma$ (MPa)	V_0 (m yr⁻¹)	$(a - b)\sigma$ (MPa)	V_0 (m yr⁻¹)	
4-month	0.56[a]	0.084	1.84[a]	0.0200	12.14[a]
7-month	0.56[a]	0.084	1.84[a]	0.0195	12.14[a]
10-month	0.56[a]	0.084	1.84[a]	0.0175	12.14[a]
1-year	0.56[a]	0.084	1.84[a]	0.0168	12.14[a]
2-year	0.56[a]	0.084	1.84[a]	0.0114	12.14[a]
3-year	0.56	0.078	1.84	0.0090	12.14
Wang and Bürgmann (2020)	2.7	1.42	0.073	0.06	–

[a]The variable is fixed.

Figure 8. Convergence process with simulated annealing algorithms for V_0 and $(a-b)\sigma$ updip (a and b) and downdip (d and e) of the coseismic rupture, as well as the transition depth (f), based on the 3-year postseismic deformation time series. The trade-off correlation between updip V_0 and $(a-b)\sigma$ is shown in (c). The black dash-dotted line represents the optimal parameter.

rupture to explain 3-year postseismic deformation, which confirms the results of Wang and Bürgmann (2020). However, this afterslip model cannot predict the temporal evolution of the postseismic deformation well; for example, it underestimates the early postseismic deformation (Figure 7).

Our purpose is to seek a rate-strengthening afterslip model that is capable of estimating InSAR observations spatiotemporally. We attempt to verify whether the depth-varying fault friction is responsible for the underfitting of the SA-1 model in Figure 7, which is reasonable because of the weak sedimentary multilayers along depth (see Section 5.4.3). Considering that the afterslip is mainly concentrated around the updip section of the fault, there are four segments for the updip part of the coseismic rupture (seg1-4 in Figures 5a and 6a; Figure S15a in Supporting Information S1). Because more fault segments and too many searching parameters would make it difficult to obtain convergence, as well as the trade-off between $(a-b)\sigma$ and V_0 (Figure 8c), we choose to fix some parameters according to the search results of the SA-1 model (Table 1): the $(a-b)\sigma$ and V_0 of the downdip section (seg5) are fixed at 1.84 MPa and 0.009 m yr^{-1}, respectively; we force no afterslip on seg4 with V_0 to be 0 m yr^{-1} because little or no afterslip is indicated by the kinematic and SA-1 afterslip models (Figure 5 and Figure S15 in Supporting Information S1); V_0 is fixed at 0.078 m yr^{-1} for seg1 to seg3, and then $(a-b)\sigma$ is to be searched. As shown in Figure 9, the $(a-b)\sigma$ values for seg1 to seg3 are 0.58, 0.06, and 2.91 MPa, respectively. Compared with the SA-1 afterslip model which features friction contrast between up- and downdip parts of the fault, this multisegment model (herein called the SA-2 afterslip model, Figure 6) can better explain the observations (Figure 7). In addition, the sedimentary stratigraphy consists of different lithologies at different depths in this
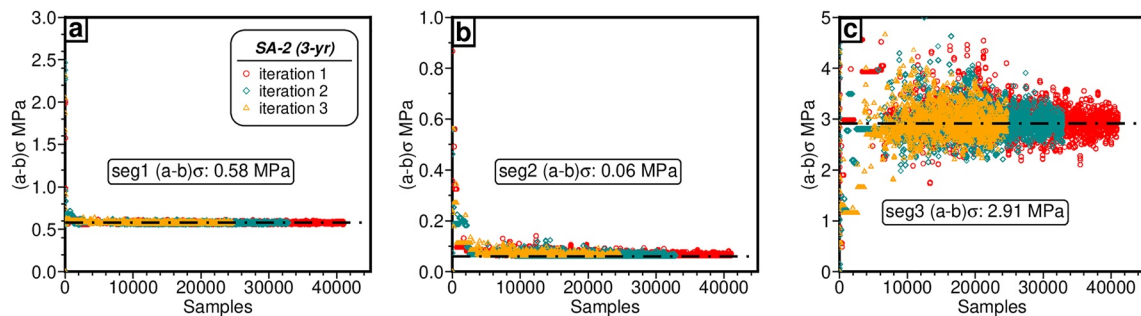

Figure 9. Convergence process with simulated annealing algorithms for $(a-b)\sigma$ of seg1-3 updip of the coseismic rupture. The black dash-dotted line represents the optimal parameter.
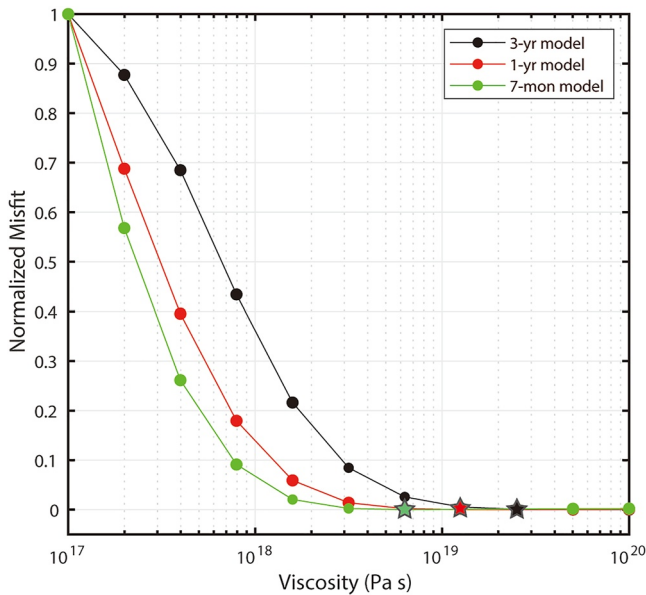
Figure 10. Trade-off between the normalized misfit of the 7-month, 1-year, and 3-year postseismic observations and viscosities. Green, red and black stars represent the best viscosity based on 7-month, 1-year, and 3-year postseismic observations, respectively.

region, for example, limestones, shales, marls, evaporites, and sandstones at depths ranging from 8–12 km from the Cambrian to Triassic (e.g., Casciello et al., 2009; Sadeghi & Yassaghi, 2016; Le Garzic et al., 2019, please see Section 5.4.3). Different lithological units could exert a significant control on the friction properties of the fault plane (Floyd et al., 2016; Yassaghi & Marone, 2019). Thus, even though the SA-2 model does not significantly improve the RMS (Root Mean Square) error (Figure 7), the depth-varying friction is more physically plausible given the depth-dependent mechanical stratigraphy in this region. However, there is still underfitting between the early postseismic deformation and simulations, and the 3-year postseismic deformation for ascending Track T072A is overestimated (Figure 7), which indicates that the fault friction may be more complex than we thought. We will discuss this issue in Section 5.4.

4.3. The Combination of Stress-Driven Afterslip and Viscoelastic Relaxation

The contribution of viscoelastic relaxation is still in question: Wang and Bürgmann (2020) suggested that the viscoelastic relaxation deformation within 1 year is less than 1 cm, while Lv et al. (2020) argued that the viscoelastic contribution from 6 months to 2.5 years after the mainshock is relatively significant. In this section, we attempt to explore a combined postseismic mechanism of viscoelastic relaxation and stress-driven afterslip. Based on the 7-month, 1-year, and 3-year simulations from the SA-2 afterslip model, we adopt PSGRN/PSCMP (Wang et al., 2006) to simulate the corresponding viscoelastic relaxation using a layered elastic model and by exploring a range of Maxwell viscosities (from 1×10^{17} to 1×10^{20} Pa s). The same coseismic slip distribution used for estimating stress-driven afterslip is employed to calculate viscoelastic relaxation. We find that the best-fitting viscosity is no less than 10^{19} Pa s from these three models (Figure 10), which is consistent with the best estimates of the rheological viscosity from Lv et al. (2020). However, the viscoelastic response with a viscosity on the order of 10^{19} Pa s cannot match the deformation pattern of the ascending tracks (Figure S16 in Supporting Information S1). More importantly, the maximum range change of 3-year viscoelastic relaxation for descending tracks is ~1.5 cm (Figure S16 in Supporting Information S1), which is only approximately one tenth of the 3-year cumulative LOS deformation. Our viscoelastic simulations are in good agreement with Wang and Bürgmann (2020), indicating that viscoelastic relaxation is unlikely to be a dominant postseismic mechanism.

4.4. Analysis of the Downdip Afterslip

Given that the viscoelastic response is negligible, afterslip should therefore be the dominant postseismic deformation source. The postseismic slip models derived from some previous studies (e.g., Barnhart et al., 2018; Feng et al., 2018; Liu & Xu, 2019) indicate no clear afterslip on the downdip section of the coseismic rupture, while Wang and Bürgmann (2020) suggested that the inferred peak afterslip in the downdip section is ~0.3 m. The kinematic and rate-strengthening afterslip models from this study also indicate smaller downdip afterslip than updip (Figures 5 and 6; Figure S15 in Supporting Information S1). In this section, a detailed analysis and discussion are performed to identify the deep afterslip downdip of the coseismic rupture.

In this study, we first removed the coseismic deformation of the two large aftershocks (Mw 5.9 earthquake on 25 August 2018 and Mw 6.3 earthquake on 25 November 2018, Figures 2a–2d) from our InSAR postseismic time series, based on the fault models proposed by Fathian et al. (2021) (Figures S3 and S4 in Supporting Information S1, also see Section 2.2). We find that the two ~M 6 aftershocks do have an influence on the afterslip models of the mainshock, especially the Mw 5.9 aftershock, which contributes to the afterslip on the downdip part of the mainshock (Figure 11). Although afterslip introduced by aftershocks is not excessive (Figure 11c), it makes the recovery of afterslip details downdip of the mainshock more challenging. In this study, therefore, the coseismic deformation of the two aftershocks is removed, but we ignore their postseismic signals because the
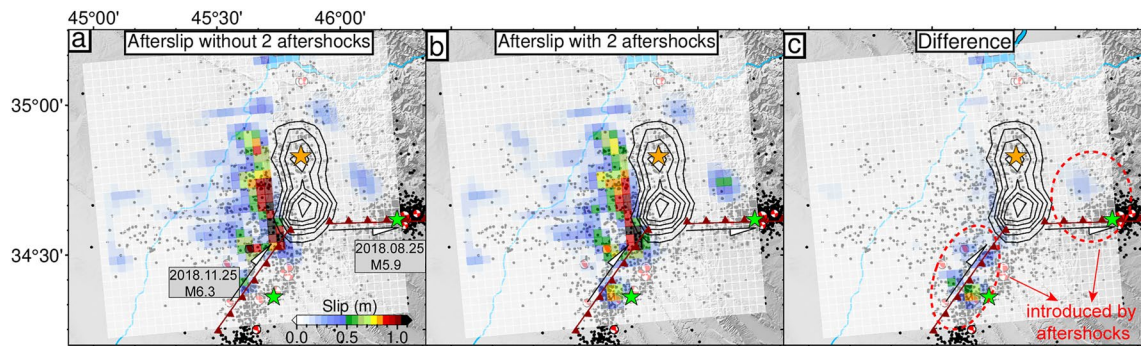
Figure 11. ~3-year kinematic afterslip models after (a) and before (b) removing the coseismic deformation of the two ~M 6 aftershocks; (c) the difference between (a and b). Black contours and orange star represent the coseismic slip model at 1-m intervals and the epicenter of the Mw 7.3 mainshock, respectively. Green stars and dark red faults represent the locations of the two large aftershocks and the corresponding fault traces from Fathian et al. (2021), respectively. The black dots and red beach balls indicate that the aftershocks are from the Iranian Seismological Center catalog.

aftershocks are much smaller than the mainshock, and it is very tricky to separate the postseismic deformation of the aftershocks from that of the mainshock. After reducing the localized signal contamination of the aftershocks, we attempt to analyze the downdip afterslip from the perspective of the data accuracy and model resolution.

As the topography grows from west to east (Figure 2g) in the Zagros, the surface deformation downdip of the coseismic rupture may be contaminated by topography-correlated atmospheric noise. Even though we reduced the atmospheric noise with GACOS (Yu et al., 2018), we first compare the noise levels of ~1-year cumulative postseismic observations between our results and those of Wang and Bürgmann (2020). We mask the deformation field and select nondeforming areas in the ~1-year descending and ascending InSAR observations from Wang and Bürgmann (2020) and our study (Figure S17 in Supporting Information S1) to calculate far-field deformation, which can be regarded as residual noise after corrections. Our residual noise level is slightly higher than that of Wang and Bürgmann (2020), with residual noises of ~13 and ~8 mm from both studies, respectively (Figure S17 in Supporting Information S1). Then, we quantitatively analyze how much influence residual atmospheric noise would exert on the postseismic afterslip, particularly the afterslip downdip of the coseismic rupture. We generate 100 simulations perturbed with far-field noise based on four-track InSAR observations to estimate the standard deviation from 100 afterslip distributions. The standard deviation could reflect the absolute variability of slip affected by observation noise on every slip patch. Our results show that the observation noise has more influence on the strike-slip components than on the dip-slip components (Figure 12). Although the slip uncertainties downdip of the coseismic rupture (maximum ~0.1 m) are much smaller than those of the updip section (maximum ~0.2 m), the maximum afterslip is ~0.3 and ~1.2 m for the downdip and updip sections of the coseismic rupture (Figures 5 and 6), respectively. Thus, the observation noise could lead to more significant slip errors on the downdip section than updip section of the coseismic rupture and could make it more difficult
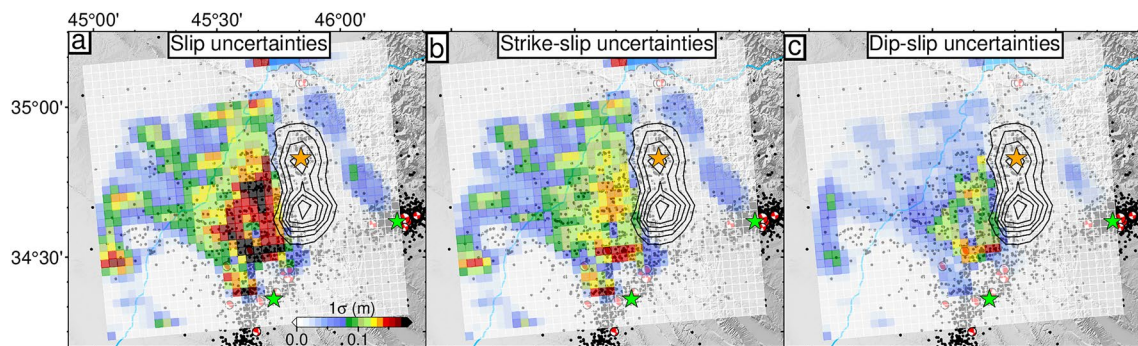
Figure 12. Standard deviation calculated with 100 perturbed datasets to simulate the influence of observation noise on model slip. (a–c) Total slip uncertainties, strike- and dip-slip uncertainties, respectively. Black contours and orange star represent the coseismic slip model at 1-m intervals and the epicenter of the Mw 7.3 mainshock, respectively. Green stars represent the locations of the two ~M 6 aftershocks. The black dots and red beach balls indicate that the aftershocks are from the Iranian Seismological Center catalog.

Figure 13. Checkerboard tests for the postseismic model resolution. The input models with ~0.6-m (a) and ~0.4-m (e) slip are used for simulating synthetic surface displacements. The slip patterns (b and f), and dip- (c and g) and strike-slip (d and h) components are r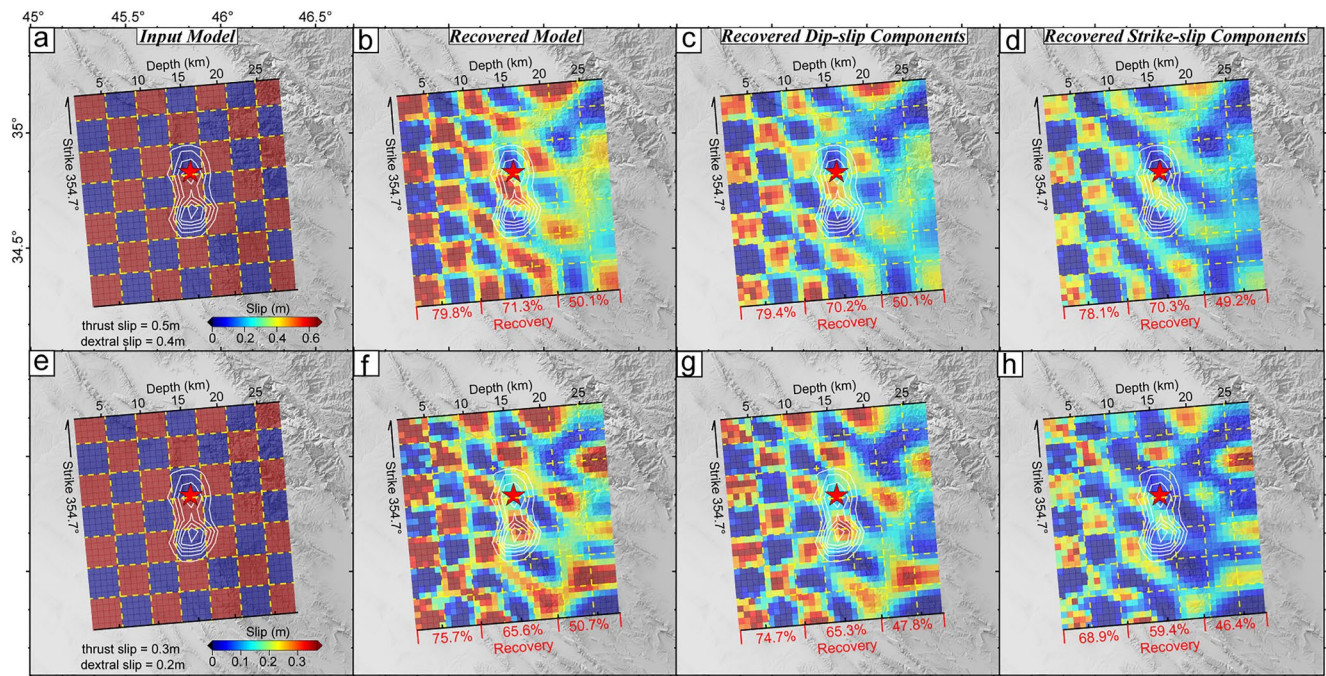ecovered by synthetic InSAR displacements. The recovery is defined as $\text{recovery} = \left(1 - \frac{\sum_{i=1}^{n}|S_i - S'i|}{\sum_{i=1}^{n}|S_i|}\right) \times 100\%$, where S_i and $S'i$ represent the input slip and inverted slip of the ith patch, respectively, and n is the number of patches with input slip.

to distinguish the downdip afterslip, which may explain the absence of the downdip afterslip derived from some previous studies (e.g., Barnhart et al., 2018; Feng et al., 2018; Liu & Xu, 2019). Overall, both our kinematic and stress-driven afterslip models indicate the existence of downdip afterslip (Figures 5 and 6 and Table 1), which confirms the results from Wang and Bürgmann (2020). The differences in downdip slip amplitudes between this study and Wang and Bürgmann (2020) may be partly due to the slightly higher noise level of our observations.

Apart from the slip uncertainties from InSAR data noise, the fault model resolution, that is, checkerboard tests with ~0.6- and ~0.4-m slips also indicates that the afterslip resolution downdip of the coseismic rupture would be lower with smaller and deeper fault slips (Figure 13). Similar to the coseismic checkerboard resolution tests (Text S2 in Supporting Information S1), we carry out the postseismic checkerboard tests based on the postseismic downsampled points (Figure S10 in Supporting Information S1) but with smaller fault slip (~0.6-m and ~0.4-m, Figure 13), which is similar to the afterslip magnitude downdip of the coseismic rupture. Our results show that the recovery is only ~50% below depth of 20 km (Figure 13). Rather than being precisely located, the slip asperities in the downdip direction of the coseismic rupture tend to be smeared over several subpatches, which suggests the decreased resolving power of downdip slip as the depth increases. Overall, without considering the influence of the aftershocks, clearly distinguishing the downdip afterslip would strongly rely on the data noise level and model resolution.

Stress-driven afterslip models could also provide valuable insights into the evolution of downdip afterslip. For the stress-driven afterslip model (SA-1 model), because of the trade-off between $(a-b)\sigma$ and V_0 (Figure 8c), we fix $(a-b)\sigma$ with 0.56 and 1.84 MPa for updip and downdip part of the fault, respectively (Table 1), and search for the V_0 with the time series of the 4-, 7-, 10-month and 1-, 2-year postseismic deformation. The results show that as the afterslip relaxes the coseismic stress changes, the downdip V_0 decays rapidly (Table 1, Figures S18–S22 in Supporting Information S1), which may be attributed to the short-term existence of the downdip afterslip. Compared with the almost invariant $(a-b)\sigma$ and V_0 of the updip section, the variation in V_0 may also indicate that the friction property evolves with time.
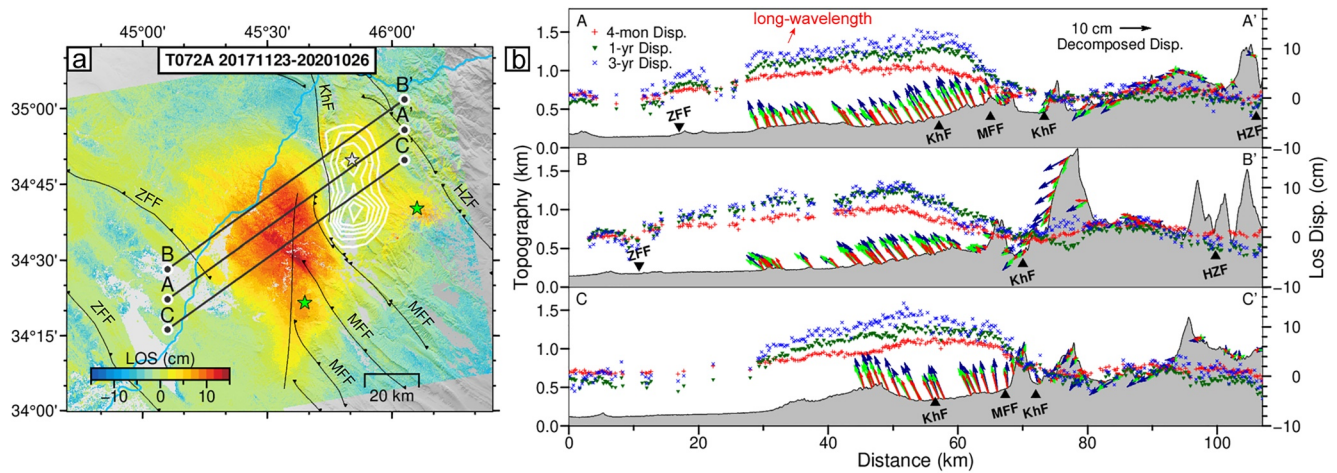
Figure 14. (a) ~3-year cumulative postseismic deformation of ascending Track T072A. White contours and gray star represent the coseismic slip model at 1-m intervals and the epicenter of the Mw 7.3 mainshock, respectively. The green stars are the two ~M 6 aftershocks. (b) Contribution of postseismic deformation to topography along Profile AA', BB', and CC' in (a). The red, green and dark blue vectors are the 2.5-dimension deformation (quasi-eastward and quasi-upward) 4 months, 1 year, and 3 years after the mainshock, respectively, which are decomposed from ascending Track T072A and descending Track T079D.

5. Discussion

5.1. Postseismic Deformation and Topographic Growth

The basement-involved faulting is found to significantly contribute to the topography growth and crustal shortening across the foreland of the mountain range via postseismic deformation. The 2.5-dimension deformation fields decomposed from ascending Track T072A and descending Track T079D indicate a long-wavelength postseismic deformation (~80 km) along Profile AA' (Figures 2a–2d and 2g, Figure 14). The decomposed 2.5-dimension deformation is consistent with the simulations of the kinematic afterslip model (Figures 2g–2h), although the decomposed displacements neglect the south-north component because of the near-polar satellite orbits. In Figures 2g and 14, postseismic deformation clearly contributes to the topography uplift west of MFF (from ZFF to MFF), while minor subsidence occurs east of the MFF (from MFF to HZF). The westward movements across these faults highlight the aseismic contribution to the crustal shortening in the foreland part of the Zagros.

Afterslip could continue for several decades after the mainshock (e.g., Zhou et al., 2018) and such long-lived postseismic slip may be related to the fold growth. Daout et al. (2021) proposed kinematic folding models which feature anelastic fold buckling to explain the shallow, long-term (more than 10 years), short-wavelength postseismic deformation of Mw ~6 thrust earthquakes in the North Qaidam fold-and-thrust system. For the 2017 Sarpol-e Zahab earthquake, however, the longer-wavelength postseismic signals may indicate deeper postseismic deformation sources (Figure 14), while the shorter-term (~3 years in this study) postseismic observations may mainly be attributed to localized afterslip or more complex deep structures. We will discuss the reactivation of the complex structures in Section 5.4. Regarding the contribution of distributed aseismic deformation to surface growth, longer postseismic observations may be needed to help us have a better understanding whether there is long-lived postseismic contribution to the topography growth in this region (Daout et al., 2021).

5.2. Comparison With Previous Afterslip Models

5.2.1. Kinematic Afterslip Models

The studies from Barnhart et al. (2018) and Wang and Bürgmann (2020) using approximately 4-month and 1-year postseismic deformation, respectively, support a ramp-and-flat structure beneath the foreland of the Zagros. Both the studies suggested significant afterslip concentrated on the shallowly dipping (~1°–10°) flat updip of the coseismic rupture. In this study, we use 4-, 7-, 10-, 12-, 24-, and 36-month postseismic data to search the postseismic fault structure. Our results confirm that the dip angle of the updip afterslip plane should be lower than 10° and that the data have limited resolution for smaller dip angles. Dutta et al. (2021) recently proposed a Bayesian

method to simultaneously estimate the non-planar fault geometry and the distributed fault slip, which may be helpful for parameterizing the refined fault geometry. However, in this study, we choose not to do more investigations about the fault geometry and we propose a ramp-flat fault to model the spatiotemporal evolution of the postseismic deformation, given the depth of basal decollement in this region. Barnhart et al. (2018) and Wang and Bürgmann (2020) indicate the optimal afterslip depth is ∼10–14 km, which is also similar to our study as models in our study with a transition depth at ∼12 km yield minimum data misfit (Figure 4 and Figure S13). Our kinematic afterslip models also favor a minor deep afterslip, which is in agreement with Wang and Bürgmann (2020).

5.2.2. Stress-Driven Afterslip Models

Compared with four parameters searched for by Wang and Bürgmann (2020) with Bayesian inversion, we initially searched for five constitutive parameters of the rate-strengthening afterslip model which consists of two fault segments (SA-1 afterslip model) with a simulated annealing algorithm. However, we find a multisegment fault model with lateral friction variation (SA-2 afterslip model) could better explain the spatiotemporal evolution of the postseismic deformation, which indicates that there is not only the friction contrast between the updip and downdip parts of the fault plane (Wang & Bürgmann, 2020), but also a depth-varying friction heterogeneity along the fault plane.

For the two-segment SA-1 afterslip model, however, our preferred results are different from those of Wang and Bürgmann (2020). Based on the 1-year postseismic deformation, Wang and Bürgmann (2020) determined that the best values of V_0 and $(a - b)\sigma$ are 1.42 m yr^{-1} and 2.7 MPa for the updip part, 0.06 m yr^{-1} and 0.073 MPa for the downdip part, respectively, which is very different from ours: 0.078 m yr^{-1} and 0.56 MPa for the updip part, 0.0090 m yr^{-1} and 1.84 MPa for the downdip part, respectively (Table 1). Such a difference may partly result from the trade-off of V_0 and $(a - b)\sigma$ (Figure 8c), which is also suggested by Wang and Bürgmann (2020). The trade-off between V_0 and $(a - b)\sigma$ is expected as equivalent V on the fault patches would be produced with low values of V_0 or high values of $(a - b)\sigma$ (see Equation 3). This strong trade-off would lead to non-unique solutions and make it difficult to distinguish the models. Furthermore, the real physical meaning of V_0 may be rather complex (e.g., Barbot et al., 2009; Perfettini & Avouac, 2007). Given such a strong trade-off and the ambiguity of the physical meanings of the constitutive parameters, either $(a - b)\sigma$ or V_0 is usually chosen to be fixed in some studies (e.g., Tian et al., 2020, 2021).

To examine the data sensitivities for these constitutive parameters of the two-segment SA-1 afterslip model, we fixed V_0 and $(a - b)\sigma$ with 1.0 m yr^{-1} and 3.0 MPa for the updip part and, 0.5 m yr^{-1} and 3.0 MPa for the downdip part, respectively, at a transition depth of 12 km, to obtain the evolution of the simulations. Then, we add Gaussian noise with 1-cm standard deviation (Figure S17 in Supporting Information S1) to the simulations to get the perturbed simulations which are used as "observations" for searching for the parameters. First, we search for the up- and down-dip V_0 with the transition depth and up- and downdip $(a - b)\sigma$ fixed; then the up- and downdip $(a - b)\sigma$ is searched with the transition depth and up- and downdip V_0 fixed. The results show that, under the disturbance of observation noise, the constitutive parameters can converge to the original values rapidly (Figures S23 and S24 in Supporting Information S1), which indicates that the existing noise level may not affect the convergence of the parameters. Therefore, without considering the observation noise, the difference in the searched parameters between this study and Wang and Bürgmann (2020) may be attributed to the strong trade-off between V_0 and $(a - b)\sigma$, the difference in InSAR observations used for searching as well as the difference in the input coseismic model and the fault configuration used for stress-driven afterslip modeling.

5.3. The Location of Afterslip and the Contribution From Viscoelastic Flow

Afterslip is a rather complex physical process and is not yet been clearly understood. In the framework of the rate-and-state friction law, the coseismic rupture usually initiates and propagates in the velocity-weakening area and its propagation tends to be impeded by the shallower unconsolidated sediments. This sediment layer with velocity-strengthening properties then would be strongly loaded and drives afterslip in consequence (Marone et al., 1991). At the downdip direction of the coseismic rupture at midcrustal depths, a transition of fault friction from velocity-weakening stick slip to velocity-strengthening brittle creep would be expected because the temperature increases with depth (e.g., Marone, 1998; Perfettini & Avouac, 2004). However, ductile flow may also be activated at depth (e.g., lower crust or upper mantle) where the temperature becomes high enough to produce dislocation creep (Perfettini & Avouac, 2004). Overall, as predicted by the rate-and-state dependent friction
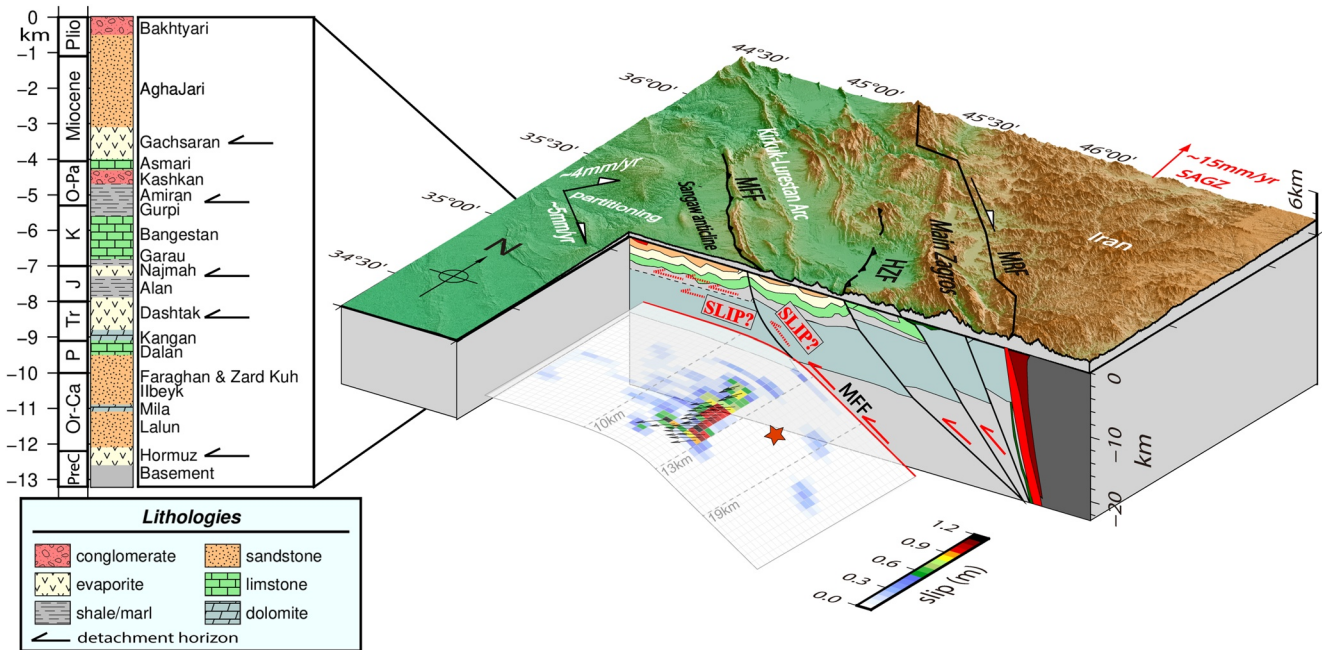
Figure 15. 3-D block diagram showing the tectonics, fault geometry, kinematic afterslip of 3 years after the mainshock and stratigraphic column in northwestern Zagros. The geological cross-section data is from National Iranian Oil company. The GPS velocity (SAGZ site) is from Khorrami et al. (2019). The simplified stratigraphic profile with approximate depths for Lurestan Salient is modified and referred from previous studies: Casciello et al. (2009), Vergés et al. (2011), Sadeghi and Yassaghi (2016), and Le Garzic et al. (2019). Red star represents the epicenter of the 2017 Sarpol-e Zahab earthquake. Stratigraphy ages and main faults are abbreviated as follows: Plio, Pliocene; O-Pa, Oligocene-Eocene-Paleocene; K, Cretaceous; J, Jurassic; Tr, Triassic; P, Permian; Or-Ca, Ordovician-Cambrian; PreC, PreCambrian; MRF: Main Recent Fault; HZF: High Zagros Fault; MFF: Mountain Front Fault.

law, in most cases afterslip tends to occur at the periphery of the coseismic rupture, where slip deficit is left by mainshocks.

For some thrust earthquakes that share tectonic settings similar to the 2017 Sarpol-e Zahab earthquake, such as the 1999 Chi-chi, 2005 Kashmir and 2015 Gorkha earthquakes, the significant afterslip occurred in the downdip portion of the fault, in conjunction with possible viscoelastic relaxation (e.g., Diao et al., 2021; Hsu et al., 2002; Wang & Fialko, 2014, 2015, 2018; Zhao et al., 2017). However, a much smaller deep afterslip downdip of the coseismic rupture than updip (Figures 5 and 6; Figure S15 in Supporting Information S1) is required by our kinematic and mechanical afterslip models for this 2017 Sarpol-e Zahab event; the viscoelastic response is also negligible, as the estimated viscosity should be greater than 10^{19} Pa s, which confirms the result from Wang and Bürgmann (2020). The existence of minor downdip afterslip is physically reasonable (e.g., Diao et al., 2021; Zhao et al., 2017) because of the velocity-strengthening frictional properties at depths below the coseismic rupture. The prominent afterslip updip of the coseismic rupture from our afterslip models coincides with the strong frictional contrast between the updip and downdip portions of the fault. Such frictional contrast may correspond to stratigraphic relations between sedimentary cover and crystalline basement (Figure 15). The transition depth from both the kinematic and rate-strengthening afterslip models is convergent to 12–13 km which also agrees well with the Hormuz evaporites according to stratigraphic profiles of this region (Figure 15, e.g., Casciello et al., 2009; Vergés et al., 2011), indicating the possible depth of cover-basement interface. Chen et al. (2018) performed joint inversion using satellite radar and teleseismic data and found the coseismic rupture velocity is more rapid downdip (~3.2 km/s) of the fault than updip (~1.5 km/s), which supports the assumption that the mainshock ruptured the cover-basement interface and was impeded by the updip sedimentary rocks. Subsequently, the loose sediments with velocity-strengthening properties are more prone to driving afterslip (Marone et al., 1991). The existence of such a low friction interface due to the transition between different geological units may be the reason that the spatial location of afterslip following the 2017 Sarpol-e Zahab event was different from other events that shared similar tectonic settings.

5.4. The Underfitting of Stress-Driven Afterslip Models

The spatiotemporal pattern of postseismic slip for the 2017 Sarpol-e Zahab earthquake may be even more complex. As shown in Figure 7, the rate-strengthening afterslip model tends to underestimate the earlier part of the postseismic deformation west of the deformation field for T072A and T079D (blue dashed boxes in Figure 7). Such far-field underfitting is unlikely to be attributed to poroelastic rebound and viscoelastic relaxation, because the former mainly contributes to near-field range changes (e.g., Peltzer et al., 1998) while the latter is negligible. The signal contamination from the two ~M 6 aftershocks, that is, the 2018 Mw 5.9 event and the Mw 6.3 event, can also be ruled out because it is far from the northwestern deformation area along Profile AA' (Figures 2 and 14). Given our afterslip inversions, geological data and local structures, some inferences about this underfitting are discussed below:

5.4.1. A More Complex Frictional Heterogeneity of Fault Plane

Compared with the stress-driven afterslip models, the kinematic afterslip model can explain the deformation spatiotemporally (Figure 7), which may be due to a more complex spatial heterogeneity of frictional properties of the fault rock. In this study, we divide the fault into five segments with different frictional properties and we have to fix some constitutive parameters, otherwise, too many search parameters would make it difficult to simulate the postseismic deformation. Even though such a multisegment model with depth-varying fault friction is proposed, the real frictional properties along the fault may be even more complex. Liu and Xu (2019) studied the co- and postseismic fault slip based on the logarithmic model which can be associated with the simple 1-D spring-slider analog model (e.g., Marone et al., 1991), and then they discussed the frictional properties of the seismogenic fault of the 2017 Sarpol-e Zahab earthquake. They derived a complex distribution of the friction parameter $a - b$ of the fault plane, even though the result would strongly rely on the priori assumptions of model parameters (e.g., the average thickness of the velocity-strengthening region). In this study, the rate-strengthening regime is a steady-state approximation of the complete rate-and-state friction law, the trade-off between V_0 and $(a - b)\sigma$ as well as the ambiguity of their physical meanings make the characterization of the fault rheology a difficult challenge, while the number of parameters of the complete rate-and-state friction law may be too large to reliably estimate (e.g., the afterslip of the Nias, Parkfield and Denali earthquakes in full rate-and-state law analyzed by Helmstetter & Shaw, 2009). Hence, in this paper, we choose not to give a more in-depth discussion about the frictional strength of the fault based on the rate-and-state friction law.

5.4.2. The Reactivation of the Blind Mountain Front Fault

With the integration of geological field data, seismic reflection profiles and well data, Tavani et al. (2018) concluded that the 2017 mainshock ruptured along the blind MFF which also matches our geological cross section data well (Figure 15). The reactivated MFF and the inherited structures break through the basal basement to the sedimentary cover in the vicinity of the mainshock (Figure 15), and are supposed to be responsible for the multiple geological structures triggered during the mainshock, for example, the Miringeh fault (Tavani et al., 2018; Figure 2g). Such a thrusting system is also considered as one of the folding mechanisms (e.g., Alavi, 2007; McQuarrie, 2004) and has been constructed to model the anticline evolution on the top of MFF in Lurestan Arc (Emami et al., 2010). Thus, except for the significant postseismic slip occurred on the cover-basement interface at the depth of ~12 km indicated by our kinematic and stress-driven afterslip models, the updip portion of the MFF or the inherited structures in sedimentary cover may also have been reactivated by the mainshock and possible postseismic slip was triggered there (Figure 15).

5.4.3. Triggered Slip on the Shallower Detachment Horizons

O'Brien (1950) first subdivided the Zagros vertical profile into five major structural units from shallow to deep: incompetent group, upper mobile group, competent group, lower mobile group and basement group. Even though the "competent group" at depths of ~5–10 km was established by this mechanical stratigraphy, multiple weak detachment horizons, often of shales, marls or evaporites, are present from northwest to southeast of Lurestan salient (Figure 15; e.g., Casciello et al., 2009; Le Garzic et al., 2019; Sadeghi & Yassaghi, 2016). The weak sedimentary multilayers in which the folds and thrust faults developed are prone to deform and directly control the distribution and processes of the folds in this region (Casciello et al., 2009; Vergés et al., 2011). Thus, we suggest the rupture of the 2017 Sarpol-e Zahab earthquake may have propagated across these decoupling horizons. A similar interpretation by Copley et al. (2015) was suggested for the 2014 Mw 6.2 Mormori earthquake in

this region. The possible triggered postseismic slip on the local detachments (Figure 15) may further couple and contribute to the fold evolutions within the sedimentary cover. The structural interpretation for this assumption is that the stress changes due to the 2017 mainshock were not fully decoupled by the low friction interface (Hormuz unit) at the cover-basement transition, and then propagated upward into the incompetent detachment levels along MFF (Figure 15). Overall, the basement thrusting system may pierce into the Phanerozoic cover and multiple decoupling layers are involved and triggered by the mainshock (Figure 15). Thus, the two-layer decoupled model would be not enough to interpret the complex interaction between the thin-, thick-skinned shortening and the seismicity in the Zagros (e.g., Barnhart et al., 2018; Wang & Bürgmann, 2020). The 2017 Sarpol-e Zahab event may be regarded as a representative example in the Zagros which contributes to both the thick- and thin-skinned shortening in seismic and aseismic ways.

6. Conclusion

The 2017 Mw 7.3 Sarpol-e Zahab earthquake is the largest instrumentally recorded event to have ruptured in the ZFTB. The co- and postseismic models associated with this event are investigated with InSAR observations in this study. The main conclusions of this work are as follows:

1. Linear inversions reveal a planar fault which is capable of explaining the coseismic deformation better than the listric faults. The coseismic rupture highlights a unilaterally southward rupture involving sequential rupture of two asperities along a dextral-thrust fault.
2. The kinematic afterslip model can predict the spatiotemporal variations in the postseismic deformation well. A multi-segment stress-driven afterslip model which features depth-varying friction is required to better explain the evolution of postseismic deformation, compared with a two-segment stress-driven afterslip model. The transition depth inverted from kinematic afterslip and rate-strengthening afterslip models is ~12 km, which can be best explained by the cover-basement interface.
3. The best-fitting viscosity based on the combination mechanisms of viscoelastic relaxation and stress-driven afterslip models is greater than 10^{19} Pa s, in which the viscoelastic contribution to the postseismic deformation is negligible.
4. Both the kinematic and stress-driven afterslip models feature minor afterslip (~0.3 m) downdip of the coseismic rupture, although resolving it clearly would strongly rely on data accuracy and model resolution.
5. The mismatch between the early postseismic deformation west of deformation field and stress-driven afterslip simulations can be explained either by a more complex spatial heterogeneity of frictional property of the fault rock, or by triggered slip on more complex geological structures, for example, the updip of MFF and the inherited structures, as well as the multiple detachment horizons there.

Data Availability Statement

The Sentinel-1 data is copyright of European Space Agency and provided by Alaska Satellite Facility (ASF, https://www.asf.alaska.edu). Aftershock data can be obtained from Iranian Seismological Center (IRSC, http://irsc.ut.ac.ir) and Global Centroid Moment Tensor (GCMT) (GCMT, https://www.globalcmt.org). Co- and post-seismic deformation used in this study are archived at Zenodo (https://doi.org/10.5281/zenodo.7113073).

References

Alavi, M. (2007). Structures of the Zagros fold-thrust belt in Iran. *American Journal of Science*, *307*(9), 1064–1095. https://doi.org/10.2475/09.2007.02

Allen, M. B., Saville, C., Blanc, E. J. P., Talebian, M., & Nissen, E. (2013). Orogenic plateau growth: Expansion of the Turkish-Iranian Plateau across the Zagros fold-and-thrust belt. *Tectonics*, *32*(2), 171–190. https://doi.org/10.1002/tect.20025

Barbot, S., Fialko, Y., & Bock, Y. (2009). Postseismic deformation due to the Mw 6.0 2004 Parkfield earthquake: Stress-driven creep on a fault with spatially variable rate-and-state friction parameters. *Journal of Geophysical Research*, *114*(B7), B07405. https://doi.org/10.1029/2008JB005748

Barbot, S., Moore, J. D. P., & Lambert, V. (2017). Displacement and stress associated with distributed anelastic deformation in a half-space. *Bulletin of the Seismological Society of America*, *107*(2), 821–855. https://doi.org/10.1785/0120160237

Barnhart, W. D., Brengman, C. M. J., Li, S., & Peterson, K. E. (2018). Ramp-flat basement structures of the Zagros Mountains inferred from co-seismic slip and afterslip of the 2017 Mw7.3 Darbandikhan, Iran/Iraq earthquake. *Earth and Planetary Science Letters*, *496*, 96–107. https://doi.org/10.1016/j.epsl.2018.05.036

Barnhart, W. D., & Lohman, R. B. (2013). Phantom earthquakes and triggered aseismic creep: Vertical partitioning of strain during earthquake sequences in Iran. *Geophysical Research Letters*, *40*(5), 819–823. https://doi.org/10.1002/grl.50201

Berardino, P., Fornaro, G., Lanari, R., & Sansosti, E. (2002). A new algorithm for surface deformation monitoring based on small baseline differential SAR interferograms. *IEEE Transactions on Geoscience and Remote Sensing*, *40*(11), 2375–2383. https://doi.org/10.1109/TGRS.2002.803792

Berberian, M. (1995). Master "blind" thrust faults hidden under the Zagros folds: Active basement tectonics and surface morphotectonics. *Tectonophysics*, *241*(3–4), 193–224. https://doi.org/10.1016/0040-1951(94)00185-c

Casciello, E., Vergés, J., Saura, E., Casini, G., Fernández, N., Blanc, E., et al. (2009). Fold patterns and multilayer rheology of the Lurestan Province, Zagros simply folded belt (Iran). *Journal of the Geological Society*, *166*, 947–959. https://doi.org/10.1144/0016-76492008-138

Chen, K., Xu, W., Mai, P. M., Gao, H., Zhang, L., & Ding, X. (2018). The 2017 Mw 7.3 Sarpol Zahāb earthquake, Iran: A compact blind shallow-dipping thrust event in the mountain front fault basement. *Tectonophysics*, *747–748*, 108–114. https://doi.org/10.1016/j.tecto.2018.09.015

Copley, A., Karasozen, E., Oveisi, B., Elliott, J. R., Samsonov, S., & Nissen, E. (2015). Seismogenic faulting of the sedimentary sequence and laterally variable material properties in the Zagros Mountains (Iran) revealed by the August 2014 Murmuri (E. Dehloran) earthquake sequence. *Geophysical Journal International*, *203*(2), 1436–1459. https://doi.org/10.1093/gji/ggv365

Daout, S., Parsons, B., & Walker, R. (2021). Post-earthquake fold growth imaged in the Qaidam basin, China, with Interferometric synthetic aperture radar. *Journal of Geophysical Research: Solid Earth*, *126*(3), e2020JB021241. https://doi.org/10.1029/2020JB021241

Diao, F., Wang, R., Xiong, X., & Liu, C. (2021). Overlapped postseismic deformation caused by afterslip and viscoelastic relaxation following the 2015 Mw 7.8 Gorkha (Nepal) earthquake. *Journal of Geophysical Research: Solid Earth*, *126*(3), e2020JB020378. https://doi.org/10.1029/2020JB020378

Dutta, R., Jónsson, S., & Vasyura-Bathke, H. (2021). Simultaneous Bayesian estimation of non-planar fault geometry and spatially-variable slip. *Journal of Geophysical Research: Solid Earth*, *126*(7), e2020JB020441. https://doi.org/10.1029/2020JB020441

Emami, H., Vergés, J., Nalpas, T., Gillespie, P., Sharp, I., Karpuz, R., et al. (2010). Structure of the Mountain Front Flexure along the Anaran anticline in the Pusht-e Kuh Arc (NW Zagros, Iran): Insights from sand box models. *Geological Society, London, Special Publications*, *330*(1), 155–178. https://doi.org/10.1144/SP330.9

Falcon, N. L. (1969). Problems of the relationship between surface structure and deep displacements illustrated by the Zagros Range. *Geological Society of London, Special Publications*, *3*, 9–21. https://doi.org/10.1144/GSL.SP.1969.003.01.02

Farr, T. G., Rosen, P. A., Caro, E., Crippen, R., Duren, R., Hensley, S., et al. (2007). The shuttle radar topography mission. *Reviews of Geophysics*, *45*(2), RG2004. https://doi.org/10.1029/2005RG000183

Fathian, A., Atzori, S., Nazari, H., Reicherter, K., Salvi, S., Svigkas, N., et al. (2021). Complex co- and postseismic faulting of the 2017–2018 seismic sequence in western Iran revealed by InSAR and seismic data. *Remote Sensing of Environment*, *253*, 112224. https://doi.org/10.1016/j.rse.2020.112224

Feng, W., Li, Z., Elliott, J. R., Fukushima, Y., Hoey, T., Singleton, A., et al. (2013). The 2011 Mw 6.8 Burma earthquake: Fault constraints provided by multiple SAR techniques. *Geophysical Journal International*, *195*(1), 650–660. https://doi.org/10.1093/gji/ggt254

Feng, W., Samsonov, S., Almeida, R., Yassaghi, A., Li, J., Qiu, Q., et al. (2018). Geodetic constraints of the 2017 Mw7.3 Sarpol Zahab, Iran earthquake, and its implications on the structure and mechanics of the northwest Zagros thrust-fold belt. *Geophysical Research Letters*, *45*(14), 6853–6861. https://doi.org/10.1029/2018GL078577

Floyd, M. A., Walters, R. J., Elliott, J. R., Funning, G. J., Svarc, J. L., Murray, J. R., et al. (2016). Spatial variations in fault friction related to lithology from rupture and afterslip of the 2014 South Napa, California, earthquake. *Geophysical Research Letters*, *43*(13), 6808–6816. https://doi.org/10.1002/2016GL069428

Helmstetter, A., & Shaw, B. E. (2009). Afterslip and aftershocks in the rate-and-state friction law. *Journal of Geophysical Research*, *114*(B1), B01308. https://doi.org/10.1029/2007JB005077

Hooper, A., Segall, P., & Zebker, H. (2007). Persistent scatterer interferometric synthetic aperture radar for crustal deformation analysis, with application to Volcán Alcedo, Galápagos. *Journal of Geophysical Research*, *112*(B7), B07407. https://doi.org/10.1029/2006JB004763

Hsu, Y.-J., Bechor, N., Segall, P., Yu, S.-B., Kuo, L.-C., & Ma, K.-F. (2002). Rapid afterslip following the 1999 Chi-Chi, Taiwan earthquake. *Geophysical Research Letters*, *29*(16), 1–4. https://doi.org/10.1029/2002GL014967

Jónsson, S., Zebker, H., Segall, P., & Amelung, F. (2002). Fault slip distribution of the 1999 Mw7.1 Hector Mine, California, earthquake, estimated from satellite radar and GPS measurements. *Bulletin of the Seismological Society of America*, *92*(4), 1377–1389. https://doi.org/10.1785/0120000922

Khorrami, F., Vernant, P., Masson, F., Nilfouroushan, F., Mousavi, Z., Nankali, H., et al. (2019). An up-to-date crustal deformation map of Iran using integrated campaign-mode and permanent GPS velocities. *Geophysical Journal International*, *217*(2), 832–843. https://doi.org/10.1093/gji/ggz045

Kirkpatrick, S., Gelatt, C. D., & Vecchi, M. P. (1983). Optimization by simulated annealing. *Science*, *220*(4598), 671–680. https://doi.org/10.1126/science.220.4598.671

Le Garzic, E., Vergés, J., Sapin, F., Saura, E., Meresse, F., & Ringenbach, J. C. (2019). Evolution of the NW Zagros Fold-and-Thrust Belt in Kurdistan Region of Iraq from balanced and restored crustal-scale sections and forward modeling. *Journal of Structural Geology*, *124*, 51–69. https://doi.org/10.1016/j.jsg.2019.04.006

Liu, X., & Xu, W. (2019). Logarithmic model joint inversion method forcoseismic and postseismic slip: Application to the 2017Mw7.3 Sarpol Zahāb earthquake, Iran. *Journal of Geophysical Research: Solid Earth*, *124*(11), 12034–12052. https://doi.org/10.1029/2019JB017953

Lv, X., Amelung, F., Shao, Y., Ye, S., Liu, M., & Xie, C. (2020). Rheology of the Zagros Lithosphere from post-seismic deformation of the 2017 Mw7.3 Kermanshah, Iraq, earthquake. *Remote Sensing*, *12*, 2032. https://doi.org/10.3390/rs12122032

Marone, C. J. (1998). Laboratory-derived friction laws and their application to seismic faulting. *Annual Review of Earth and Planetary Sciences*, *26*(1), 643–696. https://doi.org/10.1146/annurev.earth.26.1.643

Marone, C. J., Scholtz, C. H., & Bilham, R. (1991). On the mechanics of earthquake afterslip. *Journal of Geophysical Research*, *96*(B5), 8441–8452. https://doi.org/10.1029/91JB00275

McQuarrie, N. (2004). Crustal scale geometry of the Zagros fold-thrust belt, Iran. *Journal of Structural Geology*, *26*(3), 519–535. https://doi.org/10.1016/j.jsg.2003.08.009

Molinaro, M., Leturmy, P., Guezou, J. C., Frizon de Lamotte, D., & Eshraghi, S. A. (2005). The structure and kinematics of the southeastern Zagros fold-thrust belt, Iran: From thin-skinnedned to thick-skinnedned tectonics. *Tectonics*, *24*(3), TC3007. https://doi.org/10.1029/2004TC001633

Motagh, M., Bahroudi, A., Haghighi, M. H., Samsonov, S., Fielding, E., & Wetzel, H. U. (2015). The 18 August 2014 Mw 6.2 Mormori, Iran, earthquake: A thin-skinnedned faulting in the Zagros Mountain inferred from InSAR measurements. *Seismological Research Letters*, *86*(3), 775–782. https://doi.org/10.1785/0220140222

Mouthereau, F., Lacombe, O., & Vergés, J. (2012). Building the Zagros collisional orogen: Timing, strain distribution and the dynamics of Arabia/Eurasia plate convergence. *Tectonophysics*, *532*, 27–60. https://doi.org/10.1016/j.tecto.2012.01.022

Nissen, E., Ghods, A., Karasözen, E., Elliott, J. R., Barnhart, W. D., Bergman, E. A., et al. (2019). The 12 November 2017 Mw 7.3 Ezgeleh-Sarpolzahab (Iran) earthquake and active tectonics of the Lurestan Arc. *Journal of Geophysical Research: Solid Earth*, *124*(2), 2124–2152. https://doi.org/10.1029/2018JB016221

Nissen, E., Tatar, M., Jackson, J. A., & Allen, M. B. (2011). New views on earthquake faulting in the Zagros fold-and-thrust belt of Iran. *Geophysical Journal International*, *186*(3), 928–944. https://doi.org/10.1111/j.1365-246X.2011.05119.x

O'Brien, C. A. E. (1950). Tectonic problems of the oil field belt of southwest Iran. In: In J. Buiter (ed.) *Proceedings of 18th International Geological Congress* (Vol. *6*, pp. 45–58).

Peltzer, G., Rosen, P., Rogez, F., & Hudnut, K. (1998). Poroelastic rebound along the Landers 1992 earthquake surface rupture. *Journal of Geophysical Research*, *103*(B12), 30131–30145. https://doi.org/10.1029/98JB02302

Perfettini, H., & Avouac, J.-P. (2004). Postseismic relaxation driven by brittle creep: A possible mechanism to reconcile geodetic measurements and the decay rate of aftershocks, application to the Chi-Chi earthquake, Taiwan. *Journal of Geophysical Research*, *109*(B2), B02304. https://doi.org/10.1029/2003jb002488

Perfettini, H., & Avouac, J. P. (2007). Modeling aftership and aftershocks following the 1992 Landers earthquake. *Journal of Geophysical Research*, *112*(B7), B07409. https://doi.org/10.1029/2006JB004399

Sadeghi, S., & Yassaghi, A. (2016). Spatial evolution of agros collision zone in Kurdistan, NW Iran: Constraints on Arabia–Eurasia oblique convergence. *Solid Earth*, *7*(2), 659–672. https://doi.org/10.5194/se-7-659-2016

Talebian, M., & Jackson, J. (2004). A reappraisal of earthquake focal mechanisms and active shortening in the Zagros mountains of Iran. *Geophysical Journal International*, *156*(3), 506–526. https://doi.org/10.1111/j.1365-246X.2004.02092.x

Tavani, S., Parente, M., Puzone, F., Corradetti, A., Gharabeigli, G., Valinejad, M., et al. (2018). The seismogenic fault system of the 2017 Mw 7.3 Iran-Iraq earthquake: Constraints from surface and subsurface data, cross-section balancing, and restoration. *Solid Earth*, *9*(3), 821–831. https://doi.org/10.5194/se-9-821-2018

Tian, Z., Freymueller, J. T., & Yang, Z. (2020). Spatio-temporal variations of afterslip and viscoelastic relaxation following the Mw 7.8 Gorkha (Nepal) earthquake. *Earth and Planetary Science Letters*, *532*, 116031. https://doi.org/10.1016/j.epsl.2019.116031

Tian, Z., Freymueller, J. T., & Yang, Z. (2021). Postseismic deformation due to the 2012 Mw 7.8 Haida Gwaii and 2013 Mw 7.5 Craig earthquakes and its implications for regional rheological structure. *Journal of Geophysical Research: Solid Earth*, *126*(2), e2020JB020197. https://doi.org/10.1029/2020JB020197

Vajedian, S., Motagh, M., Mousavi, Z., Motaghi, K., Fielding, E. J., Akbari, B., et al. (2018). Coseismic deformation field of the Mw 7.3 12 November 2017 Sarpol-e Zahab (Iran) earthquake: A decoupling horizon in the northern Zagros Mountains inferred from InSAR observations. *Remote Sensing*, *10*, 1589. https://doi.org/10.3390/rs10101589

Vergés, J., Goodarzi, M. G. H., Emami, H., Karpuz, R., Efstathiou, J., & Gillespie, P. (2011). Multiple detachment folding in Pusht-e Kuh Arc, Zagros: Role of mechanical stratigraphy. *AAPG Memoir*, *94*, 69–94. https://doi.org/10.1306/13251333M942899

Vernant, P., Nilforoushan, F., Hatzfeld, D., Abbassi, M. R., Vigny, C., Masson, F., et al. (2004). Present-day crustal deformation and plate kinematics in the Middle East constrained by GPS measurements in Iran and northern Oman. *Geophysical Journal International*, *157*(1), 381–398. https://doi.org/10.1111/j.1365-246X.2004.02222.x

Walpersdorf, A., Hatzfeld, D., Nankali, H., Tavakoli, F., Nilforoushan, F., Tatar, M., et al. (2006). Difference in the GPS deformation pattern of North and Central Zagros (Iran). *Geophysical Journal International*, *167*(3), 1077–1088. https://doi.org/10.1111/j.1365-246X.2006.03147.x

Wang, K., & Bürgmann, R. (2020). Probing fault frictional properties during afterslip updip and downdip of the 2017 Mw 7.3 Sarpol-e Zahab earthquake with space geodesy. *Journal of Geophysical Research: Solid Earth*, *125*(11), e2020JB020319. https://doi.org/10.1029/2020JB020319

Wang, K., & Fialko, Y. (2014). Space geodetic observations and models of postseismic deformation due to the 2005 M7.6 Kashmir (Pakistan) earthquake. *Journal of Geophysical Research: Solid Earth*, *119*(9), 7306–7318. https://doi.org/10.1002/2014JB011122

Wang, K., & Fialko, Y. (2015). Slip model of the 2015 Mw 7.8 Gorkha (Nepal) earthquake from inversions of ALOS-2 and GPS data. *Geophysical Research Letters*, *42*(18), 7452–7458. https://doi.org/10.1002/2015GL065201

Wang, K., & Fialko, Y. (2018). Observations and modeling of coseismic and postseismic deformation due to the 2015 Mw 7.8 Gorkha (Nepal) earthquake. *Journal of Geophysical Research: Solid Earth*, *123*(1), 761–779. https://doi.org/10.1002/2017JB014620

Wang, R., Lorenzo-Martín, F., & Roth, F. (2006). PSGRN/PSCMP—A new code for calculating co- and post-seismic deformation, geoid and gravity changes based on the viscoelastic-gravitational dislocation theory. *Computers & Geosciences*, *32*(4), 527–541. https://doi.org/10.1016/j.cageo.2005.08.006

Wegmüller, U., Werner, C., Strozzi, T., Wiesmann, A., Frey, O., & Santoro, M. (2015). Sentinel-1A support in the GAMMA software, proceedings of fringe 2015 workshop, Frascati, Italy, 23–27 March.

Wessel, P., & Smith, W. H. (1998). New, improved version of generic mapping Tools released. *Eos, Transactions American Geophysical Union*, *79*(47), 579. https://doi.org/10.1029/98EO00426

Xu, G., Xu, C., Wen, Y., & Yin, Z. (2019). Coseismic and postseismic deformation of the 2016 Mw 6.2 Lampa earthquake, Southern Peru, constrained by interferometric synthetic aperture radar. *Journal of Geophysical Research: Solid Earth*, *124*(4), 4250–4272. https://doi.org/10.1029/2018JB016572

Yang, Y. H., Hu, J. C., Yassaghi, A., Tsai, M. C., Zare, M., Chen, Q., et al. (2018). Midcrustal thrusting and vertical deformation partitioning constraint by 2017 Mw 7.3 Sarpol Zahab earthquake in Zagros Mountain Belt, Iran. *Seismological Research Letters*, *89*(6), 2204–2213. https://doi.org/10.1785/0220180022

Yassaghi, A., & Marone, C. (2019). The relationship between fault zone structure and frictional heterogeneity, insight from faults in the High Zagros. *Tectonophysics*, *762*, 109–120. https://doi.org/10.1016/j.tecto.2019.04.029

Yu, C., Li, Z., Penna, N. T., & Crippa, P. (2018). Generic atmospheric correction model for interferometric synthetic aperture radar observations. *Journal of Geophysical Research: Solid Earth*, *123*(10), 9202–9222. https://doi.org/10.1029/2017JB015305

Zhao, B., Bürgmann, R., Wang, D., Tan, K., Du, R., & Zhang, R. (2017). Dominant controls of downdip afterslip and viscous relaxation on the postseismic displacements following the Mw7.9 Gorkha, Nepal, earthquake. *Journal of Geophysical Research: Solid Earth*, *122*(10), 8376–8401. https://doi.org/10.1002/2017JB014366

Zhou, Y., Thomas, M. Y., Parsons, B., & Walker, R. T. (2018). Time-dependent postseismic slip following the 1978 Mw 7.3 Tabas-e-Golshan, Iran earthquake revealed by over 20 years of ESA InSAR observations. *Earth and Planetary Science Letters*, *483*, 64–75. https://doi.org/10.1016/j.epsl.2017.12.005

References From the Supporting Information

Ding, K., He, P., Wen, Y., Chen, Y., Wang, D., Li, S., & Wang, Q. (2018). The 2017 Mw 7.3 Ezgeleh, Iran earthquake determined from InSAR measurements and teleseismic waveforms. *Geophysical Journal International*, *215*(3), 1728–1738. https://doi.org/10.1093/gji/ggy371

Feng, W., Li, Z., Hoey, T., Zhang, Y., Wang, R., Samsonov, S., et al. (2014). Patterns and mechanisms of coseismic and postseismic slips of the 2011 Mw 7.1 Van (Turkey) earthquake revealed by multi-platform synthetic aperture radar interferometry. *Tectonophysics*, *632*, 188–198. https://doi.org/10.1016/j.tecto.2014.06.011

Feng, W., Lindsey, E., Barbot, S., Samsonov, S., Dai, K., Li, P., et al. (2017). Source characteristics of the 2015 MW 7.8 Gorkha (Nepal) earthquake and its MW 7.2 aftershock from space geodesy. *Tectonophysics*, *712–713*, 747–758. https://doi.org/10.1016/j.tecto.2016.02.029